ADVANCING EARTH AND SPACE SCIENCES

Geochemistry, Geophysics, Geosystems

RESEARCH ARTICLE
10.1029/2025GC012808

Coupling UV Camera-Derived SO_2 Emission Rate and Thermal Output at Mount Etna: A Decadal Analysis Across Eruptive Phases

Giovanni Lo Bue Trisciuzzi[1], Alessandro Aiuppa[1], Marcello Bitetto[1], Mauro Coltelli[2], Francesco Ciancitto[2], Gaetana Ganci[2], Mimmo Palano[1,2], Giuseppe Bilotta[2], Emilio Pecora[2], Paolo Principato[2], Angelo Vitale[1], and Dario Delle Donne[3]

[1]Dipartimento di Scienze della Terra e del Mare (DiSTeM), University of Palermo, Palermo, Italy, [2]INGV-Osservatorio Etneo, Catania, Italy, [3]INGV-Osservatorio Vesuviano, Napoli, Italy

Key Points:

- Enhanced SO_2 degassing (above background) from UV Camera is commonly observed in temporal proximity to most of Etna's eruptive phases
- Results reveal a strong imbalance in the magma volumetric budget, with only a small fraction of degassed magma being erupted
- Variations in the stored magma volume show coherent fluctuations with vertical ground displacement of the volcano edifice

Supporting Information:

Supporting Information may be found in the online version of this article.

Correspondence to:

G. Lo Bue Trisciuzzi,
giovanni.lobuetrisciuzzi@unipa.it

Citation:

Lo Bue Trisciuzzi, G., Aiuppa, A., Bitetto, M., Coltelli, M., Ciancitto, F., Ganci, G., et al. (2026). Coupling UV Camera-derived SO_2 emission rate and thermal output at Mount Etna: A decadal analysis across eruptive phases. *Geochemistry, Geophysics, Geosystems*, *27*, e2025GC012808. https://doi.org/10.1029/2025GC012808

Received 17 NOV 2025
Accepted 6 JUL 2026

Author Contributions:

Conceptualization: Giovanni Lo Bue Trisciuzzi, Alessandro Aiuppa, Gaetana Ganci, Mimmo Palano, Dario Delle Donne
Data curation: Alessandro Aiuppa, Marcello Bitetto, Mauro Coltelli, Francesco Ciancitto, Gaetana Ganci, Mimmo Palano, Giuseppe Bilotta, Emilio Pecora, Paolo Principato, Angelo Vitale, Dario Delle Donne

Abstract

At persistently degassing open-vent volcanoes, SO_2 emissions are especially useful to capture the transition from quiescence to eruption, though accurate quantification is challenged by complex volcanic plume dynamics and limited resolution of observations. Here, we present an exceptionally long (~10–year) record of SO_2 emission rates from the Etna volcano in Italy, obtained using a permanent UV Camera system. We combine these data with satellite-derived thermal fluxes to explore the links between SO_2 degassing, thermal output, and eruptive behavior. We initially used the thermal flux to identify the main eruptive phases during 2015–2024. For each of these phases, we identify a typical increasing pattern in time-averaged SO_2 fluxes, from ~2,000 t/d during inter-eruptive periods, to ~2,500 t/d in the days before (and after) eruptions, to ~3,800 t/d during eruptions. Coupling thermal-derived magma output rates with SO_2-derived magma supply rates, we quantify the volumetric imbalance between supplied and erupted magma. Results show that only ~28% of the eruptible magma (i.e., the volume of magma in excess to that sustaining background activity) is discharged during eruptions, with the remaining magma fraction (~72%) being stored intrusively. We additionally calculate that ~120 Mm^3 of magma (or more, considering that the UV-Camera derived SO_2 emission rates are likely minimum estimates) may have accumulated during the 2015–2021 interval, contributing to volcano deformation. Our analysis underscores the importance of integrated gas and thermal observations for improved interpretation of monitoring data.

Plain Language Summary

Volcanic gases released from open-vent volcanoes provide essential information on the state and evolution of a magmatic system. The sulfur dioxide (SO_2) emission rate is particularly useful in volcano monitoring, as it has been proven to be a tracer of magma migration toward shallow volcano plumbing systems. In this study, we analyze ~10 years (late-2015 to 2024) of SO_2 data from Mount Etna in Italy, collected with a permanent UV Camera system, and combined them with satellite measurements of heat emitted from the volcano (a proxy for magma output rates). We found a systematic association between phases of heightened SO_2 and eruption. Converting SO_2 and thermal data into volumetric magma fluxes, we also show that only ~28% of magma supplied to the volcano is discharged during eruptions, while the remaining part is stored within the magmatic system, slowly deforming the volcano's surface. Combined gas and thermal observations can improve our understanding of volcanic behavior, and can eventually help anticipate eruptive activity, hence contributing to better volcanic hazard assessment.

1. Introduction

The emission of volcanic gases at active volcanoes is the ultimate effect of magma degassing, caused by decompression and/or crystallization of magma in the subsurface (Edmonds et al., 2022; Edmonds & Wallace, 2017; Oppenheimer et al., 2014). Monitoring volcanic gases plays a crucial role in understanding magma behavior at depth, and ultimately how likely (and when) magma is to erupt (Aiuppa, Agusto, et al., 2025, Aiuppa, Caudron, et al., 2025; Edmonds, 2021). After water vapor and carbon dioxide, sulfur dioxide (SO_2) is the third most abundant volcanic gas (Oppenheimer et al., 2011), and its release is strictly linked to magma convective ascent in the upper portion of transcrustal magma plumbing systems (Scaillet et al., 1998; Shinohara, 2008), and/or to gas bubble separate ascent from shallow stored magma (Edmonds et al., 2022). As such, monitoring the SO_2 emission rate (here referred also as SO_2 flux) provides fundamental insights into volcano behavior that can contribute to volcanic hazard assessment (Arellano et al., 2021; Kern et al., 2022; Lo Bue Trisciuzzi et al., 2024;

Formal analysis: Giovanni Lo Bue Trisciuzzi, Alessandro Aiuppa, Marcello Bitetto, Mauro Coltelli, Francesco Ciancitto, Gaetana Ganci, Giuseppe Bilotta, Emilio Pecora, Paolo Principato, Angelo Vitale, Dario Delle Donne
Funding acquisition: Alessandro Aiuppa, Gaetana Ganci
Investigation: Giovanni Lo Bue Trisciuzzi, Alessandro Aiuppa, Marcello Bitetto, Gaetana Ganci, Mimmo Palano, Dario Delle Donne
Methodology: Giovanni Lo Bue Trisciuzzi, Alessandro Aiuppa, Marcello Bitetto, Mauro Coltelli, Francesco Ciancitto, Gaetana Ganci, Mimmo Palano, Giuseppe Bilotta, Emilio Pecora, Paolo Principato, Angelo Vitale, Dario Delle Donne
Project administration: Alessandro Aiuppa
Resources: Alessandro Aiuppa, Marcello Bitetto, Gaetana Ganci, Mimmo Palano, Emilio Pecora, Paolo Principato, Angelo Vitale
Software: Giovanni Lo Bue Trisciuzzi, Marcello Bitetto, Mauro Coltelli, Francesco Ciancitto, Giuseppe Bilotta, Emilio Pecora, Paolo Principato, Angelo Vitale, Dario Delle Donne
Supervision: Alessandro Aiuppa, Gaetana Ganci, Mimmo Palano, Dario Delle Donne
Validation: Alessandro Aiuppa, Marcello Bitetto, Mauro Coltelli, Francesco Ciancitto, Gaetana Ganci, Mimmo Palano, Giuseppe Bilotta, Emilio Pecora, Paolo Principato, Dario Delle Donne
Visualization: Giovanni Lo Bue Trisciuzzi, Dario Delle Donne
Writing – original draft: Giovanni Lo Bue Trisciuzzi, Alessandro Aiuppa, Gaetana Ganci, Mimmo Palano, Dario Delle Donne
Writing – review & editing: Alessandro Aiuppa, Gaetana Ganci, Mimmo Palano, Dario Delle Donne

Theys et al., 2019). Compared to the more abundant volcanic gases, SO_2 has very low natural background levels and shows distinct absorption features in the ultraviolet (UV) spectral ranges, making it relatively easy to detect with spectroscopic techniques (Kern, 2025; Oppenheimer et al., 2011).

The relevance of SO_2 in volcanology has promoted continuous technical efforts to improve the precision and accuracy of SO_2 flux records via ground-based and satellite-based remote sensing (e.g., Carn et al., 2017; Galle et al., 2003; Kantzas & McGonigle, 2008; Kern, 2025; Oppenheimer et al., 2011, 2014). The improved spatial and temporal resolution of current gas records has unveiled the intrinsically nonstationary nature of SO_2 degassing (Arellano et al., 2021; Carn et al., 2017; Fischer et al., 2019; Mori et al., 2013; Shinohara, 2013), in which periods of heightened emission alternate with period of reduced degassing (Carn et al., 2017; Kazahaya et al., 2004; Mori et al., 2013). While such fluctuations complicate the reconstruction of long-term emission inventories and the estimation of global volcanic gas budgets (Werner et al., 2019), they also open the opportunity to identify and interpret unrest at restless volcanoes (Aiuppa, Agusto, et al., 2025). Sustained increases in SO_2 emissions have often been detected in the run-up to eruption, confirming the role of this gas as a tracer of magma ascent and decompression (Aiuppa et al., 2023; Boichu et al., 2015; Kunrat et al., 2022; Laiolo et al., 2022). Moreover, integrating SO_2 flux measurements with thermal or geophysical data (e.g., Aiuppa et al., 2023; Coppola et al., 2019; Laiolo et al., 2022; Reath et al., 2019) provides valuable insights for understanding volcanic dynamics, hence contributing to more effective hazard assessment.

The advent of UV Cameras (Bluth et al., 2007; Mori & Burton, 2006) has paved the way for SO_2 flux measurements with improved spatial and temporal resolution, hence with large potentials for volcanic monitoring (Burton et al., 2015). However, these instruments typically require deployment in the proximity of the active vents that, while reducing light dilution effects (Campion et al., 2015), result in the targeting of the proximal and often most optically opaque volcanic plume portions, in which radiative transfer errors can be large (Kern, Deutschmann, et al., 2010; Kern, Kick, et al., 2010; Kern et al., 2012, 2013). Furthermore, the proximity to the active vents often causes the plume to be only partially imaged by UV cameras due to the morphological complexity of volcano summits or unfavorable wind directions (Delle Donne et al., 2022; Lo Bue Trisciuzzi et al., 2024). This, combined with challenges in site conditioning and maintenance, has made UV Cameras predominantly used for discrete surveys (Ilanko et al., 2020; Tamburello et al., 2011), while applications of permanent deployments for semi-continuous observations have so far been restricted to a limited number of volcanoes (Burton et al., 2015; D'aleo et al., 2016; Delle Donne et al., 2017; Kern et al., 2015; Wilkes et al., 2023).

Mount Etna, on the eastern coast of Sicily (Figure 1a), is one of the few volcanoes on Earth instrumented with one of such permanent UV Camera systems, since 2014 (Delle Donne et al., 2019). Etna, the largest active volcano in Europe, is known for its nearly persistent activity (Branca et al., 2011). The volcano currently reaches a maximum elevation of ∼3,400 m, and has a summit crater terrace consisting of four active craters (Figure 1b): the Voragine Crater (VOR), the Bocca Nuova Crater (BN), the Northeast Crater (NEC), and the Southeast Crater (SEC) (Branca et al., 2011). Etna's activity is primarily characterized by continuous degassing from its summit craters, driven by passive gas release from shallow convecting magma (Allard, 1997), and usually accompanied by mild Strombolian activity. However, this background activity is often interrupted by effusive eruptions (Andronico et al., 2005; Branca & Del Carlo, 2004, 2005; Branca et al., 2011) and by more energetic lava fountaining episodes (Andronico et al., 2021) that can last for hours. These short-lived episodes are generally anticipated by a progressive intensification of Strombolian activity (Viccaro et al., 2014) that then evolves into lava fountains forming eruptive columns reaching heights of up to 14 km above the craters (e.g., Corsaro et al., 2017). Since the 1980s, these explosive events have become more frequent, often occurring in clusters of multiple lava fountains (Andronico et al., 2021). These events are believed to be driven by an increasing influx of volatile-rich mafic magma into a shallow magma storage zone located at about 2–4 km depth beneath the summit. The interaction of this mafic magma with more evolved, shallower resident magma (Aiuppa et al., 2023; Corsaro et al., 2017; Giuffrida & Viccaro, 2017; Kahl et al., 2015) is believed to trigger gas-driven pressure buildup over periods ranging from days to months (Giuffrida & Viccaro, 2017), ultimately resulting in eruption (Bonaccorso et al., 2013, 2021; Cannata et al., 2018; Corsaro et al., 2017; Patanè et al., 2013).

Here, we review and discuss the utility and implications of UV Camera observations at Etna, by presenting a nearly decade-long analysis (November 2015–December 2024) of SO_2 flux results obtained by the permanent UV Camera system (Figures 1b and 1c). The SO_2 flux time series is combined with satellite-derived thermal data obtained using the SEVIRI sensor, and with volcanic activity records (Figure 2a) extracted from the INGV-OE

10.1029/2025GC012808

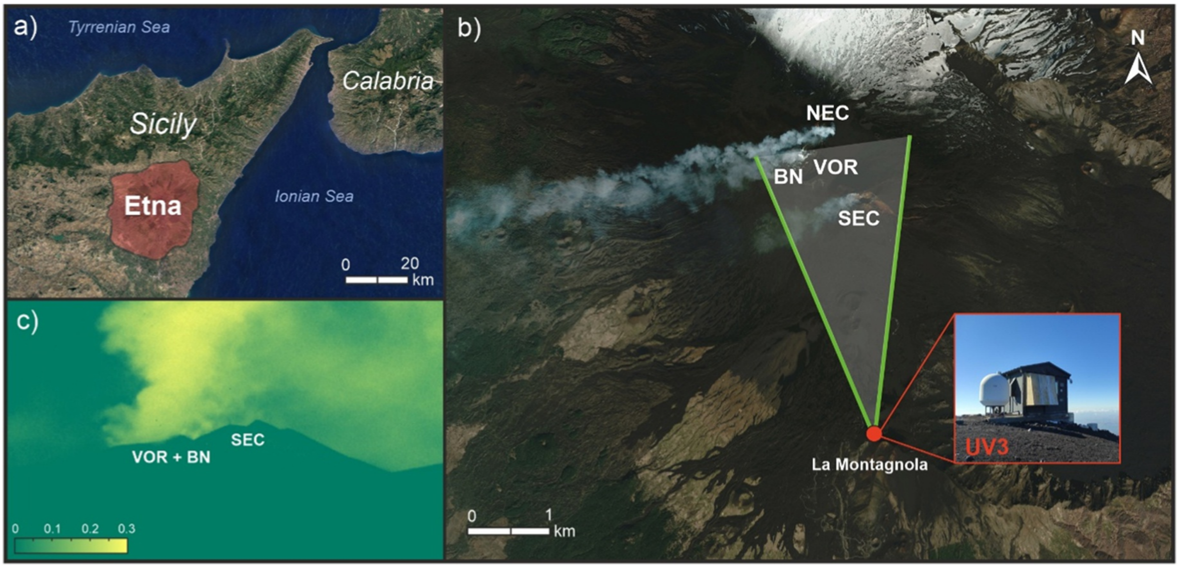

Figure 1. (a) Geographical location of Mount Etna; (b) View of the Etna's summit craters and location of the UV Camera system (UV3) at "La Montagnola" ridge. The UV Camera field of view is represented as the area encompassed between the green lines; (c) Example of absorbance image taken from the UV3 system.

(Istituto Nazionale di Geofisica e Vulcanologia—Osservatorio Etneo) monitoring reports (INGV-OE monitoring reports). The aim of this integrated analysis is to evaluate the utility of UV Camera records for the understanding of degassing dynamics at Etna, and for anticipating/tracking the quiescent-to-eruption transition.

2. Methods

2.1. SO_2 Flux Measurements From UV Camera

The daily averaged SO_2 flux time series used in this study (Figure 2b) was obtained through manual processing of images recorded by a permanent UV Camera system (here referred also as UV3 system) installed on the "La Montagnola" ridge (Figure 1b), at an elevation of 2,600 m. The system is installed within a protected INGV monitoring shelter that provides a controlled environment, enabling sustained long-term operation and continuous data acquisition since 2014. The site provides an optimal view of the southern sector of the summit crater terrace, located approximately 3 km to the north.

The system employs two JAI CM-140GE-UV Cameras sensitive to UV radiation and fitted with band-pass optical filters (Full Width at Half Maximum, FWHM, of 10 nm). Because SO_2 absorption of solar radiation decreases sharply around ~320 nm (Vandaele et al., 1994), the system employs two narrow-band filters: one covering the 300–320 nm range, corresponding to the region of maximum absorption, and one covering the 320–340 nm range, located outside the absorption band. These co-aligned cameras capture daily image sequences (520 × 676 pixels at 10-bit resolution) at a frame rate of 0.5 Hz during optimal lighting conditions (e.g., from 7:30 a.m. to 12:30 p.m. UTC). Image acquisition was automated using a Fujitsu RX100 Workstation. Details of hardware and software have been described in previous work (D'Aleo et al., 2016, 2019; Delle Donne et al., 2019).

The daily acquired images are processed using a MATLAB custom code (Delle Donne et al., 2019), where pairs of images taken simultaneously by the two cameras are merged into single absorbance images, applying the Beer-Lambert law. This method allows for the quantification of the relative absorption of scattered UV sunlight by volcanic SO_2 within the camera's field of view (FoV). The resulting SO_2 absorption images are then converted into SO_2 column density images by applying a proportionality ratio between absorbance and SO_2 column density (McGonigle, 2007).

In our processing workflow, a fixed proportionality coefficient is adopted rather than a dynamic calibration based on a co-located spectrometer. Although the system was originally designed to include a spectrometer for continuous calibration, intermittent instrumental failures and technical issues during the ~10 years of observations prevented from its application. For this reason, the calibration coefficient was determined from repeated

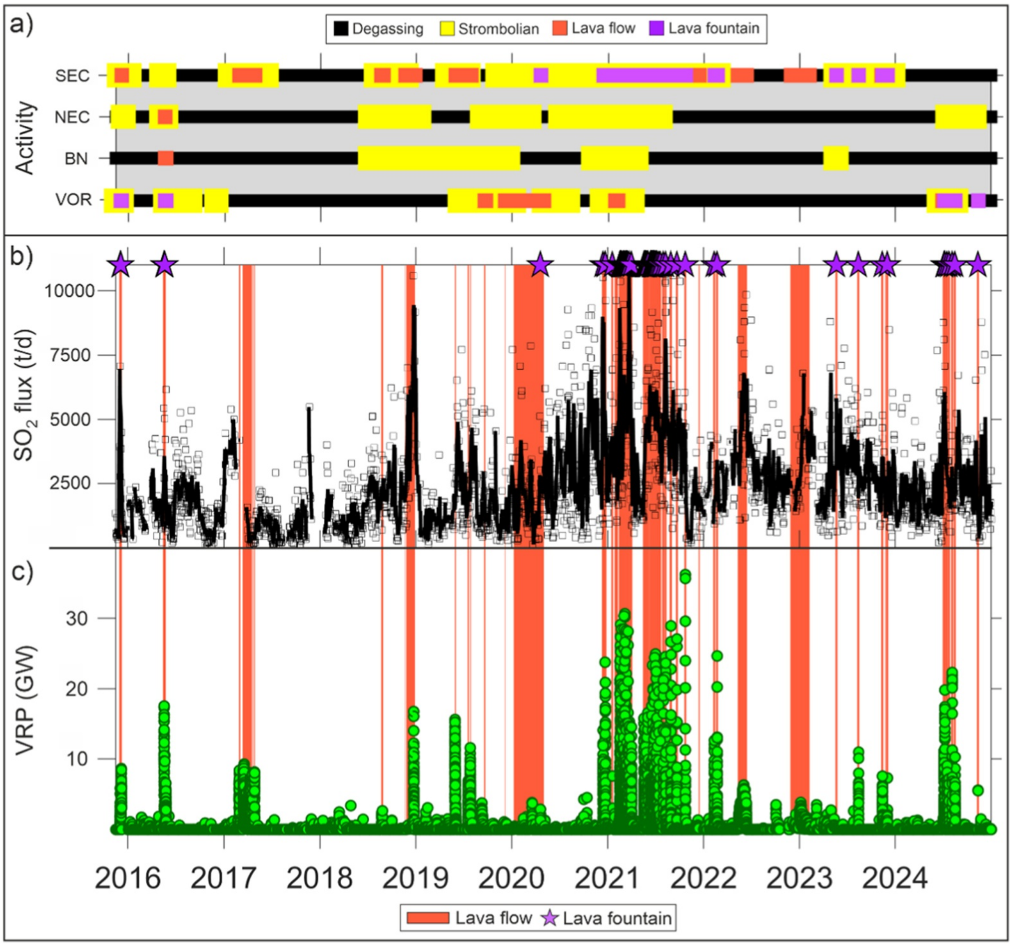

Figure 2. (a) Eruptive activity (colored squares) at Etna's summit craters, inferred from INGV-OE monitoring reports; (b) SO_2 daily averaged flux from UV Camera. Squares represent the raw data, and the black solid line represents a 7-day moving average; (c) Volcanic radiative Power (VRP) from SEVIRI images. In panels "b" and "c" are also reported, as red shaded bands/lines, all the not-ordinary eruptive events (lava flows and lava fountains) reported in panel "a."

calibration campaigns carried out using SO_2 gas cells of known column density, during the whole UV Camera operational time (spanning from 07:30 to 12:30 UTC). Examples of calibration curves are shown in Figure S1 in Supporting Information S1. These highlight that while the slope of the absorbance-SO_2 cell regression varies relatively widely between approximately 07:30 and 09:00 UTC, when illumination conditions change rapidly, they then stabilize at ∼9,000 from 09:00 UTC (green area in Figure S1 in Supporting Information S1), when variability is limited to ≤5% (expressed as 1 standard deviation). In view of these calibration results, data reported here (Figure 2b) are based on post-processing of images acquired from 09:00 UTC onwards (early morning images are systematically discarded, in order to concentrate on periods when illumination conditions are more stable). Critically, a very similar slope of ∼9,000 was observed in all calibrations performed, independently on illumination conditions (e.g., winter vs. summer; cloudy vs. sunny; see Figure S1 in Supporting Information S1), which provides confidence on our fixed proportionality coefficient approach. While we caution that a fixed calibration approach may fail short in responding to rapid changes in environmental (illumination) conditions, our focus here is on capturing the averaged (daily) flux regime, which can safely be obtained from averaging hundreds to thousands of images taken under favorable measurement and illumination conditions.

SO_2 column densities are integrated along a rectangular sub-area positioned above the crater terrace, capturing the full cross-section of the imaged plume. Although such a near-vent environment is potentially subject to the largest radiative effects (see below), its selection is motivated by the need of prioritizing analysis on plume sectors in which transport is more directly controlled by gas initial momentum and buoyancy, rather than by the wind field

(Lo Bue Trisciuzzi et al., 2024). Finally, the derived integrated SO_2 column amounts (kg/m) are multiplied by the plume speed (m/s) obtained by applying an optical flow algorithm tracking the movement of gas fronts in consecutive frames (Delle Donne et al., 2019; Lucas & Kanade, 1981), to obtain a 0.5 Hz SO_2 flux daily time series (kg/s).

Our analysis is subject to caveats and limitations. For example, cloud coverage and the presence of ash in the imaged plume can attenuate the in-plume SO_2 signal (e.g., Kern, Deutschmann, et al., 2010; Kern et al., 2013), causing the derivation of artificially low flux estimates. To mitigate against these effects, the SO_2 fluxes reported here represent daily averaged values (t/d) obtained from averaging all SO_2 fluxes associated with optimal measurement conditions during the day. Image selection is performed first using an automated visibility index (Delle Donne et al., 2019) to discard images acquired under poor observing conditions (e.g., presence of clouds, ash, or not optimal illumination conditions), which are relatively common on Etna's summit. The remaining images are then visually inspected and validated by an operator, who identifies and manually removes residual poorly acquired images that were not excluded by the automated filtering procedure. Typically, under favorable meteorological conditions, a large fraction of images is retained, whereas no image is processed in cases of persistent cloud cover at the summit. Over a typical observation year, circa 50% of the acquired images finally pass to post-processing (see Figure S2 in Supporting Information S1).

Perhaps more critically, our UV Camera targets the most proximal (Figures 1b and 1c) and hence optically densest part of the plume, making it potentially more vulnerable to errors related to multiple scattering of light within the plume, caused by aerosols, ash and water droplets (Kern, 2025; Kern, Deutschmann, et al., 2010; Kern et al., 2012, 2013). Measurements are also affected by light dilution, a process caused by scattering toward the instrument of photons that have not, or have only partially, traversed the volcanic plume (Kern, Deutschmann, et al., 2010). Since these photons do not contain spectral absorption structures, they generate an artificial dilution of the measured column density. This effect is primarily dependent on observation distance, atmospheric conditions and in-plume SO_2 content (Campion et al., 2015; Kern, Deutschmann, et al., 2010), and can weaken the SO_2 signal, resulting in a net underestimation of SO_2 column densities.

To estimate the possible effect of light dilution on our data set, we first empirically estimated the atmospheric scattering coefficient (σ) by applying the methodology described in Campion et al. (2015). Specifically, we fitted Equation 1 of Campion et al. (2015) to a 1-hour subset of image intensities measured over three portions of the volcanic edifice located at known distances from the UV Camera, selecting relatively homogeneous regions in order to minimize artifacts related to illumination and surface heterogeneity (Figure S3 in Supporting Information S1). During the fitting procedure, the initial intensity (I_0) and the atmospheric scattering coefficient (σ) were treated as free parameters, while the ambient intensity (I_A) was estimated from the mean intensity measured in a clear-sky region unaffected by volcanic gas absorption (Figure S3 in Supporting Information S1). The retrieved scattering coefficient at 310 nm yields an average value of 1.26×10^{-4} m^{-1}, slightly lower than the standard-pressure dry-air value reported by Penndorf (1957) (1.33×10^{-4} m^{-1}). We next applied the formulation (Equation 1) reported by Lübcke et al. (2013; Equation D1 in Appendix D) to our cell-calibrated images:

$$S(d) \simeq S_0 \cdot e^{-\sigma \cdot d} \quad (1)$$

where S and S_0 are the measured and true SO_2 column densities respectively, σ is the atmospheric scattering coefficient, and d is the plume-to-camera distance.

Considering a distance (d) of 3,000 m and the retrieved atmospheric scattering coefficient (σ) of 1.26×10^{-4} m^{-1}, we find that light dilution causes an average underestimation of the true SO_2 column densities of ~32% (see also Aiuppa et al., 2023). Since Equation 1 accounts only for the linear component of light dilution, this value should be regarded as a first-order (lower-bound) estimate.

To account for the increasingly non-linear light dilution effects at high SO_2 column densities (Campion et al., 2015), we take advantage of the uncorrected versus true column densities relationship in Table 1b of Campion et al. (2015). This relationship is applied at our observation distance (3 km) and interpolated to derive a second-order polynomial correction curve. At the typical range of SO_2 column densities observed at Etna (Figure S4a–S4e in Supporting Information S1), the relationship (of Figure S4f in Supporting Information S1) predicts that light dilution can cause an SO_2 attenuation of ~35% to ~55% (for SO_2 column densities of respectively

~1,000 and 3,000 ppm m) on individual pixels. Ultimately, if we apply this correction function pixel-to-pixel to a representative subset of high-flux eruptive images (January–April 2021, Figure S4g in Supporting Information S1), and then integrate the corrected pixel matrices along the entire plume cross-section (i.e., the sub-area profile above the crater terrace), we find total SO_2 flux underestimation to varies between ~30% and ~40%.

The calculation above suggests that under our field conditions, light dilution effects can be significant (30%–40% underestimation) and variable (depending on atmospheric and plume conditions; Campion et al., 2015; Kern, Deutschmann, et al., 2010). However, no explicit effort is made to apply automatic correction procedures. Rather, the linear correction of Lübcke et al. (2013) and the non-linear relationship derived from Table 1b of Campion et al. (2015) are only used to estimate the magnitude of light dilution effects. Acknowledging this methodological over-simplification, we still note that our rigorous image selection procedure, based on both the application of a visibility index and subsequent operator review, ensures that daily fluxes are derived by averaging hundreds to thousands of images acquired under optimal conditions, hence minimizing the influence of multiple scattering effects and short-term fluctuations in plume and ambient conditions.

The UV Camera's field of view (Figures 1b and 1c) also limits the detectable gas emissions to those released from the southern portion of the crater terrace, which encompasses mainly the South-East Crater (SEC) and the southern portion of central craters (VOR + BN) (D'Aleo et al., 2019). Hence, the system's configuration prevents from capturing emissions from the North-East Crater (NEC), and underestimates emissions from the central craters, except during intense explosive events that generate high sustained plumes (D'Aleo et al., 2019). As a result, our SO_2 flux measurements do not reflect the total plume emissions from Etna, which are regularly monitored with scanning UV spectrometers located at greater distances (Salerno et al., 2009).

2.2. Radiant Heat Flux From SEVIRI

Eruptive episodes at Mount Etna can be quantified from space by multispectral satellite observations (Figure 2c). Here we use the radiant heat flux (in Watts) derived from space-borne images acquired by the Spinning Enhanced Visible and InfraRed Imager (SEVIRI) sensor on board Meteosat Second Generation (MSG) satellite. The SEVIRI sensor acquires images in several regions of the electromagnetic spectrum, including the middle and thermal infrared that are particularly useful in detecting and tracking hot spots associated with high temperature events, such as fires and effusive activity (Bonaccorso et al., 2011; Hirn et al., 2008). Due to the high frequency of acquisition (~5–15 min), SEVIRI is also the most suitable space-based instrument for observing and tracking short-lived eruptive events such as Etna's lava fountains (Calvari et al., 2021, 2022; Ganci, Cappello, Bilotta, et al., 2018; Ganci, Cappello, Zago, et al., 2018; Ganci et al., 2011, 2016). Caveats and limits include the SEVIRI spatial resolution of 3 km at the nadir, which may hamper the detection of lower-intensity thermal events, such as strombolian activity, or small lava flows. On the other hand, during phases of intense volcanic activity, the SEVIRI channel (3.9 μm) designed to capture high-temperature features can become saturated, causing a possible underestimation in the recorded signal.

SEVIRI multispectral images are processed via the CL-HOTSAT system, a new version of the HOTSAT system (Ganci et al., 2011, 2016) implemented in the OpenCL standard to obtain near-real-time monitoring of volcano-related thermal activity. The CL-HOTSAT system developed at INGV-OE allows for automatic detection of thermal anomalies and quantification of thermal activity through calculation of the radiant heat flux. The system automatically downloads the SEVIRI images in near real-time using the API service provided by EUMETSAT (the Data Access API Client) using a Python-based routine and locates the thermal anomalies (hotspots) within each image, computing the radiant heat flux for each hotspot pixel. Finally, the total radiant heat flux is obtained by summing the individual radiant heat flux of all hotspot pixels for each image.

2.3. Magma Input Rate Inferred From UV Camera Measurements

Open-vent volcanoes are globally significant emitters of heat and volatiles that, during their persistent regular activity, produce more gas than explained by degassing of erupted magma (Francis et al., 1993; Kazahaya et al., 1994). Such excess degassing implies either the existence of an efficient magma convection mechanism within the volcanic plumbing system that allows huge parcels of magma to degas without being erupted (Shinohara, 2008), or an effective gas-separate ascent from stored magma (Edmonds et al., 2022). As a direct consequence, during ordinary activity, the magma supply/degassing rate (Q_{in}) into the shallower portion of the magmatic plumbing system exceeds the magma discharge rate (Q_{out}) from the active vents.

10.1029/2025GC012808

The magma supply (input) rate into the volcanic plumbing system can be quantified from SO_2 flux measurements (Aiuppa et al., 2023; Calvari et al., 2018; Coppola et al., 2019; Delbrel et al., 2024). The conversion of SO_2 flux into magma input (degassing) rates is commonly achieved using a petrological approach based on the following equation (Shinohara, 2008):

$$Q_{\text{in}} = \frac{\phi_{SO_2}}{2\Delta X_S \cdot (1 - x) \cdot p_m \cdot 86.4} \tag{2}$$

where Q_{in} represents the magma input rate (in m^3/s) above the SO_2 exsolution level (the depth at which sulfur starts to degassing from melt, typically at pressures below ~150 MPa, corresponding to depths of less than ~3 km; Métrich et al., 2010; Moretti & Papale, 2004), ϕ_{SO_2} is the SO_2 flux (in t/d), ΔX_S represents the sulfur loss during degassing (inferred from the difference between parental melt and residual post-eruption sulfur contents in Etna's magmas), and x and p_m correspond to melt crystallinity and density (in kg/m^3), respectively. The value of 86.4 is the unit's conversion factor from t/d to kg/s.

In brief, the equation establishes a connection between SO_2 emissions and the volume of magma feeding the volcanic system, providing an estimate of magma supply/degassing rates. The method relies on knowledge of the initial (pre-degassing) and final (post-emplacement) sulfur content in the melt and has been extensively applied at Mount Etna to constrain magma degassing budgets at various timescales (Allard, 1997; Allard et al., 2006; Coppola et al., 2019; D'Aleo et al., 2019; Steffke et al., 2011).

The application of Equation 2 requires a model that accurately describes sulfur (S) behavior during degassing of Etna's alkali basalts. Such a model should, starting from the known initial S content in parental magmas, predict the fraction of S lost to the vapor phase along the magma decompression path to the surface (Allard, 1997). Deeply trapped primitive melt inclusions are commonly used to estimate the initial (pre-degassing) S content of parental melts (Wallace & Edmonds, 2011). At Etna, early melt inclusion studies (Métrich et al., 2004; Spilliaert et al., 2006) indicated a parental melt S content of approximately 3,000 ppm (0.3 wt%), and a systematic sulfur loss to vapor initiating at ≤150 MPa pressures, causing up to ~95% sulfur extraction from melt ($\Delta X_S = 0.00285$; used in Aiuppa et al., 2023; Allard, 1997; Allard et al., 2006). More recent work (Gennaro et al., 2019), however, has found more variable parental melt S contents in Etna magmas. We then used Equation 2 to convert our daily averaged SO_2 fluxes (ϕ_{SO_2}) into a daily averaged magma input rates (Q_{in}) by considering the full spectrum of ΔX_S and crystallinity x values in Etna's magmas. For this aim, we used a 3,000 ppm parental melt as an upper limit scenario (ΔX_S at 0.00285 and $x = 0$), and a 2,200 ppm parental melt (from Gennaro et al., 2019) ($\Delta X_S = 0.00205$ and $x = 0.3$) as a lower limit scenario, following the same conditions used in Aiuppa et al. (2023). An intermediate scenario is then obtained by averaging the minimum and maximum estimates (see Figure S5b in Supporting Information S1). In all calculations, melt density (p_m) is fixed at 2,700 kg/m^3, as a typical density of basaltic magmas, used in various previous works at Mount Etna (e.g., Andronico et al., 2018; Del Negro et al., 2013; Greco et al., 2022). Note that, as the SO_2 flux measurements reported here do not correspond to the total bulk plume (see Section 2.1), the obtained magma input rates can approximate the total magma input rates only if/when activity is concentrated at SEC. Based on these magma supply rates, the cumulative volume of degassed magma over time can be established by integrating the supply rates over a selected period.

2.4. Magma Output Rate Using SEVIRI Thermal Anomalies

During an eruption, the radiant heat flux radiated by lava (calculated from SEVIRI images) can be converted into time-averaged discharge rate (TADR i.e. an estimation of the effusion rate, in m^3/s) adopting the relationship (e.g., Harris et al., 1997; Wright et al., 2001):

$$\text{TADR} = \frac{Q}{\rho(C_p \Delta T + C_L \Delta_\phi)} \tag{3}$$

where Q is the total thermal flux obtained by summing up the radiant heat flux computed for each hotspot pixel, ρ is the lava density, C_p is the specific heat capacity, ΔT is the difference between the eruption temperature and the temperature at which flow stops, C_L is the latent heat of crystallization, and Δ_ϕ is the volume percent of crystals that form while cooling through ΔT.

10.1029/2025GC012808

The conversion from radiant heat flux to volumetric flux depends on such lava parameters and has to be determined depending on flow conditions (Harris & Baloga, 2009; Pieri & Baloga, 1986). Since we do not usually have these source parameters for the application of Equation 3, the most appropriate approach is to adopt a range of possible values. Here, we report minimum and maximum TADR estimates by adopting the extreme values reported by Harris et al. (2000, 2007) among those suitable for Etna lavas (see also Del Negro et al., 2016; Ganci et al., 2012, 2020). An intermediate estimate was then derived by averaging these limit cases (see Figure S5b in Supporting Information S1). However, this approach is based on the implicit assumption that the heat flux is generated by an active lava flow (Dragoni & Tallarico, 2009; Harris & Baloga, 2009). Consequently, the model fails when lava is not extruded but rather retained in the vent, as in the case of open-vent activity. In such circumstances, the thermal proxy provides a minimum estimate of magma circulation (convection) at a very shallow depth, rather than effusion rates, as long as the top of the magma column is sufficiently shallow to produce thermal anomalies on the surface (Aiuppa et al., 2018; Werner et al., 2017).

For effusive events, the calculation of TADR is based on a thermal budget that assumes equilibrium between the heat retained in the eruptive volume and that radiated from the surface. This approach relies on two key assumptions: (a) the volumetric flux is proportional to the surface area of the lava flow, and (b) the lava surface cools exponentially with time and distance from the vent (Harris & Baloga, 2009). However, these assumptions are not valid for short-lived transient events such as Etna's paroxysmal episodes, during which a steady-state regime, and thus thermal equilibrium cannot be established (Garel et al., 2012). During short-lived paroxysmal events, thermal anomalies are often affected by tephra fallout and/or ash column produced during the eruptive climax, which can attenuate or obscure the signal. Conversely, when the anomaly is not obscured, the high radiant power released can easily saturate the sensor. As a result, TADR cannot always be reliably calculated during the peak fountaining phase. For such events, estimation of emplaced volumes can instead be obtained by modeling the radiant heat flux curve recorded during the cooling-dominated phase of activity (Ganci et al., 2012, 2013), by incorporating the radiating area and applying constraints on the minimum and maximum expected lava thickness for these short-lived episodes (see also Ganci et al., 2023). Volumetric uncertainty is assumed at ±30% as it derives from the radiant heat flux estimation (Ganci et al., 2016, 2023). Using this technique, we computed the dense rock equivalent volume of lava that erupted during the event and underwent cooling. To estimate the effusion rate in the case of lava fountains, we divided the volume estimated via the cooling modeling by the duration of the event to obtain a mean output rate for each paroxysmal event.

A cumulative volume of erupted magma over time can be retrieved for each estimated scenario by integrating the respective TADR values.

3. Results

3.1. Characterizing Volcanic Activity Using SO_2 Fluxes, Thermal Anomalies, and INGV-OE Monitoring Reports

Throughout the ∼10-year observation period, Etna exhibited a wide spectrum of volcanic activity behaviors, with all summit craters showing intermittent or simultaneous activity. Activity was primarily concentrated at the South-East Crater (SEC) and at Voragine (VOR), while Bocca Nuova (BN) and the North-East Crater (NEC) played a secondary role (Figure 2a). Passive degassing was frequently punctuated by episodes of strombolian activity from one of the summit craters, by effusive eruptions of variable duration, and by numerous paroxysmal lava fountain episodes (Figure 2a). Lava fountains are highly energetic but short-lived events, usually lasting only a few hours, that can either occur as isolated episodes or in clusters (eruptions periodically repeating at intervals of days/weeks) (Andronico et al., 2021). From the INGV-OE weekly reports, we identified 75 paroxysmal lava fountain events, representing the most intense yet transient form of magma eruption, and 32 lava flows of variable duration. We find that the majority of the eruptive events are separated by short (<15 days, Figure 3a) inter-event times, particularly due to the clustering of lava fountains (Andronico et al., 2021).

Our nearly decade-long data set reveals large temporal fluctuations in SO_2 fluxes (Figure 2b), with daily mean values averaging at 2,468 ± 2,090 t/d (mean ± 1 standard deviation; range: from 30 to ∼20,000 t/d). Although the UV Camera system employed may underestimate the total SO_2 output, due to its preferential view of the southern sector of the summit craters, our reported SO_2 fluxes are within the range reported previously (Boichu et al., 2015; Carn et al., 2016, 2017; Corradini et al., 2020; Grandin et al., 2024; Queißer et al., 2019; Salerno et al., 2009, 2025). Despite the oscillating and complex nature of the time series, the visual inspection of Figure 2

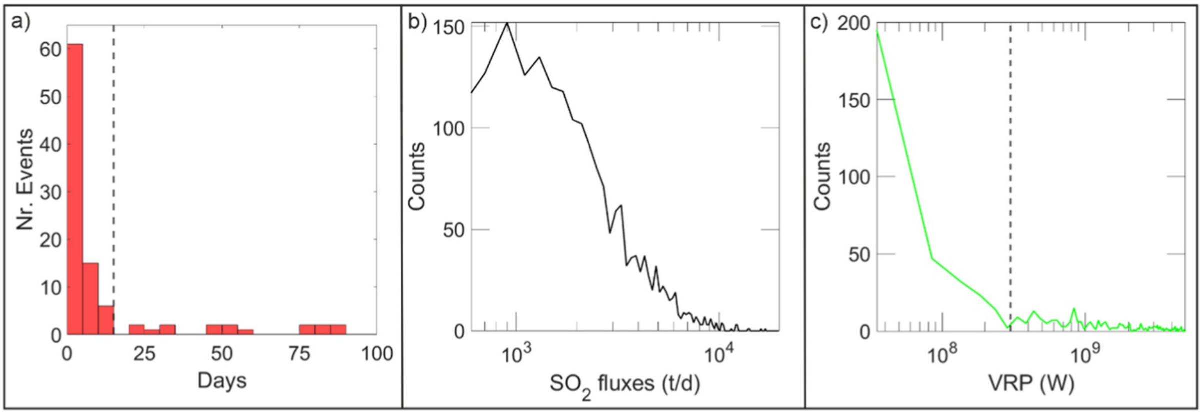

Figure 3. (a) Occurrence time between eruptive events, defined as the difference between the onset of an event and the termination of the previous one. The majority of events (~77%) show inter event times <15 days, as shown from the dashed line. (b) Distribution of daily averaged SO_2 fluxes. (c) Distribution of daily averaged VRP values. The dashed line marks two different populations, separating abundant low-VRP values from less-abundant high-VRP values.

demonstrates a broad correlation between SO_2 levels and volcanic activity state. The largest (>3,000 t/d) SO_2 fluxes are typically observed in correspondence of eruptive episodes. In particular, a systematic pattern of gradual SO_2 increase prior to eruption onset, followed by an abrupt decrease immediately after eruption cessation was evident before the 2017, late-2018, 2021, and mid-2022 eruptions (see also Figure S6 in Supporting Information S1). This pattern is, however, less evident in some other events. The lowest fluxes, typically <2,500 t/d, are recorded during phases of passive degassing and mild Strombolian activity, in what we refer to as the background persistent activity level of Etna.

The distribution of SO_2 fluxes (Figure 3b) shows an asymmetric distribution, with a peak at ~1,000 t/d. The frequency of measurements decreases progressively toward higher flux values, with a long tail extending beyond 10,000 t/d. This skewed distribution indicates that most of the measured fluxes cluster between a few hundred and a few thousand tonnes per day, whereas extreme values are comparatively rare.

Thermal anomalies detected by SEVIRI imagery (~15 min of temporal resolution) provide clear evidence of lava outpouring from vents or scoria emission from sustained Strombolian activity (Spina et al., 2025). These anomalies account for nearly 10% of the total observation time and are consistently associated with phases of elevated volcanic activity (Figure 2c). The mean VRP during the decade is 0.15 GW, with values spanning from 0 to 36 GW. Major lava fountains are mainly characterized by sharp increases in thermal output, with lava emissions typically exceeding 10 GW, whereas effusive eruptions usually provide radiant heat flux values between 1 and 10 GW, with inter-eruptive periods showing relatively stable values below 1 GW. Minor radiative peaks scattered throughout the record correspond to episodes of variable lava output that are consistently documented in daily monitoring reports.

The distribution of daily averaged radiative power shows a skewed profile (Figure 3c), with a first class of high frequency and low VRP values, and a second class of less-abundant higher VRP values at ~0.3 GW, likely marking the transition from quiescent degassing or weak Strombolian activity to more energetic eruptive behavior.

3.2. Magma Input/Output Rates

The two distinct (upper and lower scenario) magma input rates (cfr. 2.3) are illustrated by the gray banded area of Figure S5b in Supporting Information S1, together with the intermediate scenario (black line) obtained by averaging the maximum and minimum estimates. Based on the intermediate scenario, the mean magma input rate (Q_{in}) during the observed period (late-2015 to 2024) is 2.70 ± 0.89 m^3/s (expressed as the mean value ± the difference between the minimum and maximum scenarios), with a range from 0.03 to 22.3 m^3/s. The magma input rate sensibly accelerates in proximity to eruptive events, generally exceeding values >~4 m^3/s, in line with previous studies at Etna (Aiuppa et al., 2023; Allard, 1997; Allard et al., 2006; Coppola et al., 2019).

10.1029/2025GC012808

The intermediate scenario of the magma output rate is illustrated in Figure S5b in Supporting Information S1 as green triangle marks while the upper and lower scenarios are depicted as green vertical bars (cfr. 2.4). While the magma input rate generally exceeds the magma output during background (persistent) activity, this trend reverses during most eruptive events. Our output rates exhibit notable variations across a wide range of volcanic activity, spanning from 0 to >20 m^3/s during more energetic phases of lava emission, reaching the highest values during paroxysmal lava fountain events (max value: 49 m^3/s). The mean magma output rate (intermediate scenario) during the observed period is 0.40 ± 0.11 m^3/s, consistent with previous annual-averaged values (Harris et al., 2011; Wadge & Guest, 1981; Wadge et al., 1975).

4. Discussion

UV Cameras have increasingly been exploited in volcanology in the last two decades (Burton et al., 2015). Applications have been diverse, including the quantification of eruptive gas masses from small explosive events (Campion et al., 2018; Kazahaya et al., 2016; Mori & Burton, 2009), the resolution of different degassing modes (Tamburello et al., 2012), the spatial resolution of different degassing sources at multi-vent volcanoes (Delle Donne et al., 2022; Pering et al., 2020), the expedite quantification of SO_2 budgets during campaigns (Tamburello et al., 2014), and the correlation with geophysical parameters to examine the source processes controlling volcano seismicity and infrasound (Nadeau et al., 2011). In contrast, the contribution of UV Cameras to volcano monitoring has been more modest, especially because volcanoes instrumented with permanent instruments are relatively few (e.g., Stromboli: Delle Donne et al., 2017; Lo Bue Trisciuzzi et al., 2024; Kīlauea: Kern et al., 2015; Wilkes et al., 2023). Our Etna results here, with their continuity of observations, can help evaluate the potential of UV Cameras in volcano monitoring.

4.1. Can We Track Etna's Eruptive Behavior Using SO_2?

Our decadal record opens the way to quantitatively testing any possible association between SO_2 flux and volcanic activity state. To achieve this task, we use a procedure in which the eruptive events in Etna's eruption catalog during November 2015 to December 2024 ($n = 107$, 75 lava fountains + 32 lava flows; Figure 2a) are ranked based on their size, with the ensuing analysis concentrating only on a selected number of the largest events, grouped into eruptive phases. Grouping of closely spaced events into eruptive phases is motivated by the tendency of Etna's eruptions to concentrate in clusters (Andronico et al., 2021), and is a mandatory step when attempts are made to quantitatively characterize the degassing signals prior, during and after each phase—without grouping, a general overlap between pre- and post-eruptive signals produced by successive events would render degassing trends difficult to resolve.

To identify the largest events in the eruption record, we used the volcanic radiative power (VRP; Figure 2c) as a proxy for eruption magnitude. This is based on the assumption that a larger thermal output corresponds to a more sustained and voluminous eruption of lava, as the intensity of thermal emissions reveals the fractional pixel areas invaded by active flows (Harris & Baloga, 2009; Wright et al., 2001), under given compositional, insulation, rheological and ambient conditions (Harris et al., 2000, 2007, 2010). We use a VRP threshold of 0.3 GW (Figure 3c) to mark the transition between quiescent and eruptive regimes and fix the onset of an eruptive phase at the specific day where the 0.3 GW VRP threshold is first reached. Use of this VRP threshold makes resolution of quiescent versus eruptive behaviors consistent with eruptive activity reports in INGV-OE bulletins, and can be considered as a minimum transition value, since the distribution of daily averaged VRP (Figure S7 in Supporting Information S1) shows eruptive peaks consistently above 1 GW. Termination of an eruptive phase is set at the last day with VRP above the threshold, with the condition that no positive detection (VRP above threshold) is encountered in the following 30 days—if not, any additional positive detection within this interval is grouped into the same eruptive phase (see Figure S7 in Supporting Information S1). The use of a 30-day interval is motivated by the inter-event (repose) periods being <15 days for the majority (~77%) of the Etna's eruptive events (Figure 3a). Hence, a ±15-day (30 days) interval encompasses the duration of the pre- and post-eruptive periods of most of the eruptive events in the INGV-OE catalog. This procedure allows excluding from further analysis the eruptive events of shorter duration and/or reduced volume, which are unlikely to leave a detectable signal in the SO_2 flux record.

Applying this approach, and clustering events repeating at short intervals into a single phase, we identify 18 eruptive phases (marked in yellow in Figure 4 and in Figure S7 in Supporting Information S1), which broadly

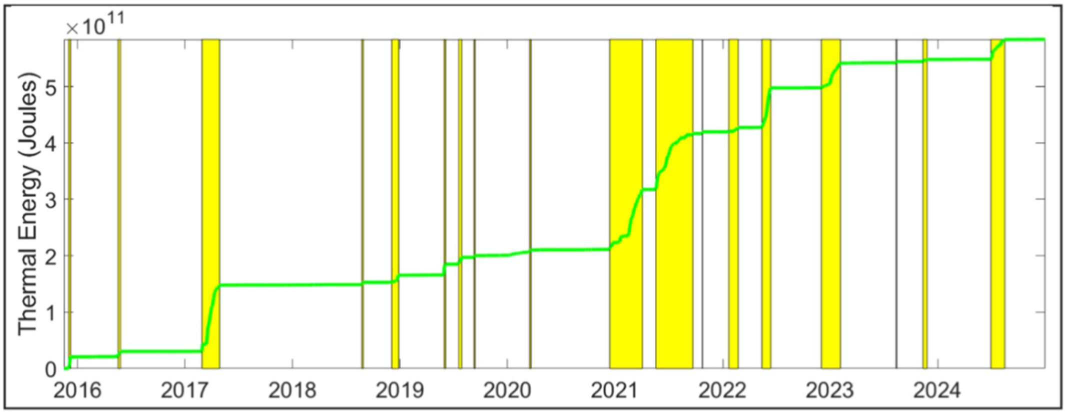

Figure 4. Main eruptive phases detected following variations in thermal radiance. The green line represents the cumulative radiant heat curve obtained by cumulating our daily averaged VRP values. The selected eruptive phases broadly follow the main steps of the cumulative thermal curve.

coincide with the main steps in the cumulative thermal curve (green line in Figure 4, derived from the thermal flux time series of Figure 2c). Each phase, reported in Table 1 with its associated thermal energy and erupted volume (obtained by integration in time of the VRP and magma output rate), corresponds to a significant short-term increase in thermal flux. Collectively, these phases account for more than 90% of the total thermal energy irradiated during the study period. Their durations range from 1 to 126 days, and the corresponding released energies range between 2.18×10^9 and 1.18×10^{11} J.

We next quantify the background SO_2 flux levels by considering all the SO_2 flux results taken in the inter-eruptive periods (Figure 5a, top panel), e.g., outside the eruptive phases defined above. The average background

Table 1
Table of Eruptive Phases Inferred From Thermal Radiance

Start	End	Duration (days)	Energy (Joules)	Volume (m^3)	Max rate (m^3/s)	Mean rate (m^3/s)
02/12/2015	09/12/2015	7	2.06E+10	2.20E+06	8.10	3.65
18/05/2016	26/05/2016	8	9.11E+09	9.89E+05	5.96	1.43
27/02/2017	28/04/2017	60	1.18E+11	1.41E+07	10.11	2.73
24/08/2018	29/08/2018	5	4.02E+09	4.09E+05	1.78	0.95
03/12/2018	27/12/2018	24	1.26E+10	1.47E+06	9.12	0.71
30/05/2019	04/06/2019	5	1.90E+10	1.94E+06	13.64	4.48
19/07/2019	29/07/2019	10	1.20E+10	1.33E+06	6.35	1.54
09/09/2019	13/09/2019	4	3.05E+09	2.98E+05	1.99	0.86
16/03/2020	21/03/2020	5	2.95E+09	3.01E+05	1.33	0.70
13/12/2020	03/04/2021	111	1.06E+11	3.30E+07	26.98	3.45
19/05/2021	22/09/2021	126	9.93E+10	4.50E+07	27.36	4.13
23/10/2021	24/10/2021	1	2.78E+09	7.15E+05	16.56	8.28
21/01/2022	22/02/2022	32	7.66E+09	9.07E+05	4.04	0.33
14/05/2022	13/06/2022	30	6.98E+10	8.25E+06	6.47	3.18
02/12/2022	05/02/2023	65	4.31E+10	5.19E+06	2.90	0.92
13/08/2023	15/08/2023	2	2.18E+09	1.78E+05	2.42	1.03
12/11/2023	26/11/2023	14	3.23E+09	3.68E+05	1.77	0.30
30/06/2024	16/08/2024	47	3.50E+10	5.78E+06	14.66	1.42

Note. Each phase is reported with its start and end dates, duration, thermal energy, involved magma volumes and its max and mean magma output rate.

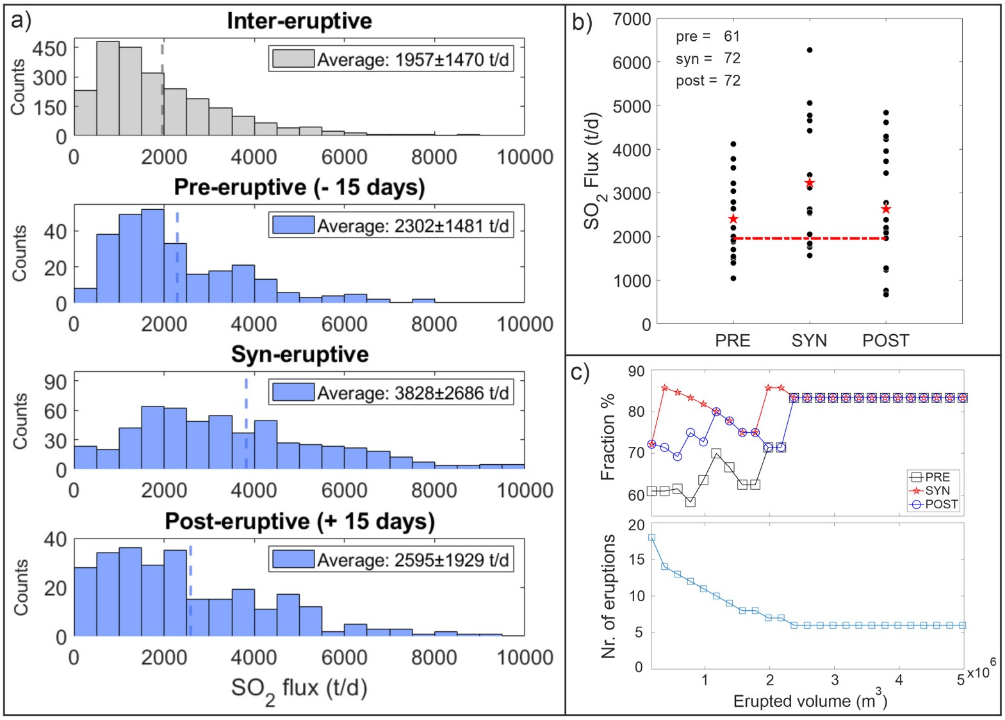

Figure 5. (a) Distribution of SO_2 fluxes from the UV Camera during inter-event and pre-, syn-, and post-eruptive periods. The dashed lines show the mean value of the distribution. (b) Fraction of eruptive phases characterized by mean SO_2 degassing above the background (inter-eruptive mean) prior, during and after each eruptive phase. Black dots show, for each eruptive phase, the mean degassing value during the pre-, syn- and post-eruptive periods. Red stars show the average value between all eruptive phases across the corresponding period. (c) Fraction of eruptive phases with mean SO_2 degassing above the background as a function of erupted volumes. The fraction generally increases progressively excluding smaller eruptions.

(e.g., inter-eruptive) Etna degassing flux for the study period is 1,957 ± 1,470 t/d (mean ± standard deviation; range, from 30 to 9,328 t/d; Figure 5a). In contrast, the syn-eruptive SO_2 flux (e.g., that corresponding to all flux results obtained with each of the 18 eruptive phases) is twice as high, averaging at 3,828 ± 2,686 t/d (Figure 5a, third panel from top). This analysis confirms that eruptions at Etna are associated with enhanced SO_2 emissions. If we concentrate on the 15-day intervals before (pre-eruptive) and after (post-eruptive) the 18 eruptive phases, we find intermediate flux levels of respectively 2,302 ± 1,481 t/d and 2,595 ± 1,929 t/d (Figure 5a, second and fourth panels from top), suggesting that major eruptive phases at Etna are broadly preceded and followed by above background SO_2 levels.

To further illustrate the variability of the SO_2 flux at, and around (before and after), an eruption, we examine the degassing trends for each of the selected eruptive phases, shown individually in Figure S8 in Supporting Information S1. This figure reveals that each of the eruptive phases considered is associated with a distinctive degassing signal. More importantly, we find that the pre-, syn- and post-eruptive flux increase is not systematic, but rather event-specific. As shown in Figure 5a, for some eruptive phases, the pre-, syn-, and post-eruptive mean fluxes fall below the quiescent (inter-eruptive) flux mean. Furthermore, the quiescent flux distribution (top panel of Figure 5a) overlaps substantially with the eruptive flux ranges (lower 3 panels of Figure 5a). Taken together, these results indicate that the quiescent versus eruptive SO_2 flux distributions are not distinctly separated, but rather broadly overlapped. This means that while the SO_2 flux allows resolving the "averaged" quiescent versus eruptive behavior, only a fraction of the eruptive phases clearly exhibits a SO_2 degassing regime well resolvable above the background.

To statistically validate these differences, we applied a two-sample Kolmogorov-Smirnov (K-S) test reporting the K-S statistic (D), which quantifies the maximum distance between the Empirical Cumulative Distribution Functions (ECDF), and the associated p-value used to assess the statistical significance. We compared the inter-eruptive SO_2 flux distribution with the pre-, syn- and post-eruptive populations. The null hypothesis of the test is

10.1029/2025GC012808

that the compared samples belong to the same statistical population. Differences between populations are considered statistically significant when the associated p-value is lower than the chosen significance level, set in this study to 0.05 (5%). Results (Figure S9 in Supporting Information S1) indicate that SO_2 emission levels during pre-eruptive ($D = 0.144$, $p << 0.05$), syn-eruptive ($D = 0.374$, $p << 0.05$), and post-eruptive ($D = 0.162$, $p << 0.05$) periods are significantly distinct from the inter-eruptive population, confirming that heightened SO_2 degassing is commonly associated with eruptive phases.

To further characterize the occurrence of enhanced degassing conditions around eruptive phases, we evaluated the fraction of pre-, syn-, and post-eruptive periods characterized by mean SO_2 fluxes exceeding the inter-eruptive level of 1,957 t/d (taken as a threshold between background vs. "perturbed" degassing conditions). Results (Figure 5b) show consistent fractions of above-background conditions across all selected eruptive phases, with values of ∼61%, ∼72%, and 72% for the subpopulations of pre-, syn-and post-eruption period, respectively. Nicely, we find that such values show a general increase for all categories with increasing eruptive volumes (Figure 5c) (e.g., when eruptive phase associated with low eruptive volumes are progressively excluded from calculation), peaking at 85% (syn-eruptive) and ∼83% (pre- and post-eruptive) for eruptive volumes between 0 and 5 Mm^3, where the majority of phases fall (∼70%, see also Figure S10 in Supporting Information S1). We conclude that while our UV Camera-derived flux record may fail to resolve the less voluminous eruptive phases from the (large) SO_2 background (sustained by passive degassing), it can easily detect more voluminous eruptive phases at Etna.

4.2. A Look Into Longer-Term (Monthly to Yearly) Thermal and SO_2 Trends

Etna's activity is known to alternate periods of heightened and reduced activity over a range of timescales (Behncke & Neri, 2003). In this section, we investigate if, and to what extent, our combined SO_2 and thermal records can capture the oscillations in volcanic activity state taking place at Etna over timescales of months to years, for example, over longer timescales than days, as investigated above (cfr. 4.1 and Figure 5). For the scope, we analyze the temporal changes in the slopes of the cumulative trends of thermal (Figure 6b) and SO_2 (Figure 6c) output, and their correlation with eruptive activity (Figure 6a).

During the late-2015 to 2024 interval, the thermal and SO_2 outputs have varied widely, as indicated by large spread of slopes of the cumulative curves (values displayed in panels b and c). The changes in the slope of the cumulative thermal energy curve (Figure 6b) match well the changes in eruptive style and energy (from INGV-OE monitoring bulletins, sequence reported in Figure 6a), supporting the ability of satellite-based thermal records to resolve between inter-eruptive and eruptive regimes. From this, and in tandem with SO_2 flux record, we can broadly identify, during the investigated period, the alternation of three main activity styles, shown with different color gradations in Figure 6.

First, we identify a year-long (from mid-2017 to mid-2018) phase of quiescence (green shaded area in Figure 6), characterized by passive degassing from summit craters (Figure 6a), and being consistently associated with the lowest thermal output (mean slope: ∼1.84 MW). Nicely, the cumulative SO_2 trend is also the flattest in this period (corresponding to an average flux of 1,054 t/d) (Figure 6c). We take this quiescent degassing period as representative of baseline (background) persistent open-vent degassing activity at Etna.

Thermal and SO_2 output excess relative to this baseline is typically associated with escalating eruptive activity. For example, periods of slightly higher thermal output (and time-averaged values below 0.3 GW; yellow shaded areas in Figure 6) contribute modestly to the overall thermal budget, and are linked to transitional eruptive behavior. This is characterized by relatively modest/infrequent eruption of magma (in which effusive and paroxysmal events are relatively modest in size), interspersed within a dominant passive degassing mode associated with mild Strombolian activity episodes from summit craters (Figure 6a). These periods include the years 2016, 2019–2020, most part of 2022, and 2023–2024. In general, intermediate SO_2 fluxes of 2,000–2,700 t/d are observed during these phases of moderate thermal energy and subdued eruptive activity.

Finally, periods of high thermal output, characterized by averaged thermal fluxes exceeding 1 GW (red areas in Figure 6), are clearly associated with more vigorous eruptive episodes. These periods encompass the 2017 and mid-2022 effusions, and the 2021 large eruptive sequence in which two main clusters of lava fountains took place (Aiuppa et al., 2023; Bruno et al., 2022; Carleo et al., 2023; Salerno et al., 2025). The 2021 sequence represents the most energetic phase of activity during the decade, and is consistently associated with a sustainedly high SO_2

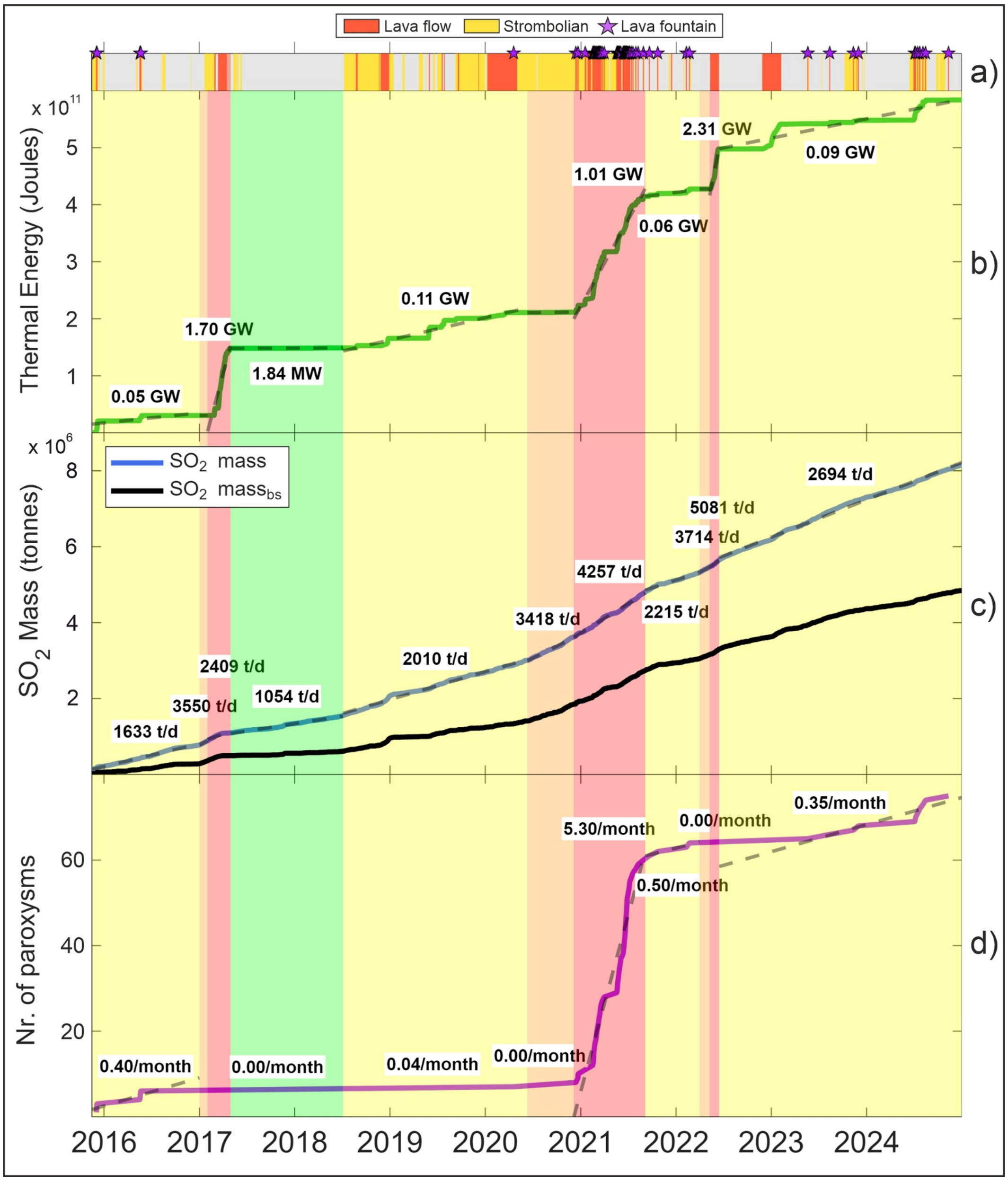

Figure 6. Main phases of volcanic activity derived from thermal radiance and SO_2 flux trends: the green area represents a phase of minor thermal energy and passive degassing from the summit crater; yellow areas represent phases of moderate thermal energy and weak and/or short-lived lava emissions; and red areas represent high thermal flux periods associated with more vigorous eruptive episodes. Orange areas represent transition phases preceding these vigorous high-thermal phases, characterized by high SO_2 fluxes. Numbers represent the average trend between phases. (a) Eruptive activity at all summit craters derived from INGV-OE monitoring reports. (b) Thermal energy derived by cumulating the daily averaged VRP values. (c) SO_2 mass obtained by cumulating the SO_2 flux (blue line) and after subtraction of the quiescent value of 1,054 t/d (SO_2 mass$_{bs}$, black line). (d) Cumulative number of paroxysms and number of monthly episodes in each phase of activity.

mass output (average SO_2 flux, 4,257 t/d; Figure 6c). During this ~9 months-long period, the largest fraction (71%) of the lava fountains occurred, with an average rate of ~5 events per month (Figure 6d).

We calculate the cumulative, background-subtracted SO_2 mass (SO_2 mass$_{bs}$; black solid line in Figure 6c) by removing from the SO_2 degassing trend the average flux (of 1,054 t/d) characteristic of the 2017–2018 quiescent degassing period. The cumulative SO_2 mass$_{bs}$ curve exhibits a segmented behavior that is broadly reminiscent of that identified from the thermal output trend (of Figure 6b). However, scrutiny of Figure 6 shows that the high-thermal phases of volcanic activity (red areas in Figure 6) are systematically anticipated by precursory slope increases in the cumulative excess SO_2 (at relatively invariant thermal output regime). These transitional phases (marked by orange shades in Figure 6) typically occur ∼1 month prior to the 2017 and mid-2022 eruptive phases, and up to ∼6 months prior to the onset of the larger 2021 eruptive sequence (Figure 6c), and are associated with average SO_2 flux values well above the background value of 1,054 t/d (or the inter-eruptive mean of 1,957 t/d) (Figure 6c). We conclude that phases of heightened SO_2 degassing predate the escalation in volcanic activity during major eruptive periods, as in 2021. This precursory SO_2 phase is interpreted to reflect the decompressional degassing of magma, resupplying the Etna's shallow plumbing system, and accumulating at depth prior to surface emplacement in a major eruptive phase/sequence (Aiuppa et al., 2023).

INGV-OE reported the occurrence of 75 paroxysmal events from November 2015 to 2024. These short-lived eruptions are characterized by the formation of ash-laden eruptive clouds several kilometres high (Calvari et al., 2021). These transient phenomena, typically lasting only a few hours, are not randomly distributed, but rather occur in clusters (Figure 6d) during periods of heightened thermal and SO_2 degassing activity (such as in 2021). Our analysis shows that our UV camera - based SO_2 flux observations have the potential to anticipate the onset of these main lava fountain clusters, with obvious benefits for volcanic hazard management in this highly touristic area.

4.3. Volumetric Magma Budget Across Different Eruptive Phases

It has long been known that a general imbalance exists between the rates of magma degassing (input) and eruption (output) at Etna (Allard, 1997) and at other volcanoes globally (Shinohara, 2008). The added value in our study is that we can characterize this imbalance not only over timescales (decades) characteristic of eruptive cycles (Allard et al., 2006) but also at the scale of individual eruptive phases, and keeping separated the different activity styles (e.g., inter-, pre-, syn- and post-eruptive periods).

We report in Figure 7 the cumulative volumes of erupted (output) and degassed (input) magma during the whole analyzed period. The volumetric magma input and output rates for all the pre, syn and post periods of the thermal-derived eruptive phases (of Figure 4) are reported in Figure S11 in Supporting Information S1. Based on the intermediate scenario (see Sections 2.4 and 3.2), results indicate that the input rates (Figure S11a in Supporting Information S1) are on average higher during the pre- and post-eruptive periods (averages of 2.58 ± 0.85 m^3/s and 2.91 ± 0.96 m^3/s; mean value ± the difference between the minimum and maximum scenarios) than during inter-eruptive periods (average 2.19 ± 0.73 m^3/s). The largest input rates are consistently observed during the syn-eruptive periods (4.30 ± 1.42 m^3/s), reflecting the same trends shown in Figure 5a. The output rates exhibit similar distributions, albeit with some distinctive features (Figure S11b in Supporting Information S1). The pre- and post-eruptive periods are characterized by very low output rates (average values of 0.012 ± 0.003 m^3/s and 0.033 ± 0.010 m^3/s respectively). In contrast, the output rates are significantly larger during the syn-eruptive periods (average 2.540 ± 0.695 m^3/s), when the main extrusion of lava takes place. This distribution confirms that the eruptive phases selected on the basis of thermal output (Figure 4 and Figure S7 in Supporting Information S1) are well constrained. The inter-eruptive magma output rate was very low (0.008 ± 0.002 m^3/s, Figure S11b in Supporting Information S1), indicating that strombolian activity contributed little to the overall erupted magma budget.

This exercise shows that, during inter-eruptive periods (passive degassing ± mild strombolian activity), only a very minor fraction ($\sim 0.4\% = 100 \times 0.008/2.198$) of the degassed magma is ultimately erupted. As the magma input rate increases (to >>2 m^3/s), the magmatic system becomes increasingly unstable, with magma overpressure build-up ultimately driving eruption (Aiuppa et al., 2023; Paonita et al., 2021). As eruption starts, the fraction of erupted magma (relative to degassing magma) then increases by more than an order of magnitude ($\sim 60\% = 100 \times 2.540/4.298$).

The same magma imbalance can be demonstrated (Figure 8) by analyzing the cumulative volumes of degassed (input) and erupted (output) magma associated with all subpopulations of inter-eruptive, pre-, syn- and post-eruptive periods (same as Figure 5). We find the largest imbalance during the inter-eruptive intervals (Figure 8), when lava extrusion from the craters is significantly reduced to the sporadic and mild Strombolian activity. In these periods, the volumetric budget is largely dominated by degassing of magma (435 ± 144 Mm^3), of which little erupted (1.33 ± 0.32 Mm^3). The pre- and post-eruptive (15-day) periods show degassed volumes of 60 ± 20 Mm^3 and 68 ± 22 Mm^3 respectively, and eruptive volumes of only 0.48 ± 0.12 Mm^3 and

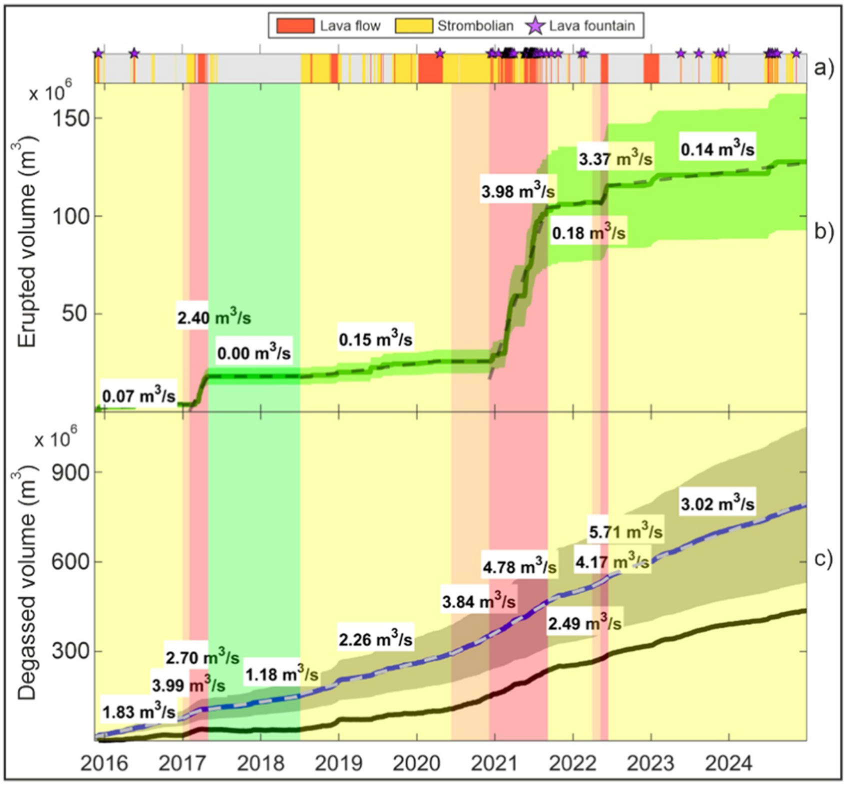

Figure 7. Cumulative volume of erupted (output) and degassed (input) magmas during the analyzed period, together with their time-averaged values during the main phases of volcanic activity inferred from thermal and SO_2 trends (cfr. 4.2); (a) Eruptive activity at all summit craters derived from INGV-OE monitoring reports. (b) Erupted magma volume derived by cumulating the magma output rates. (c) Degassed magma volume (blue line) obtained by cumulating the magma input rates. The black solid line represents the eruptible magma volume (cfr. 4.4), obtained by subtracting the baseline magma input rate of 1.18 m^3/s (green area, same as Figure 6).

1.16 ± 0.32 Mm^3, respectively. Finally, during the syn-eruptive intervals, the erupted magma volume increases significantly (∼121 ± 33 Mm^3), but still remains lower than the degassing magma volume (∼213 ± 70 Mm^3).

We conclude that magma imbalance is common to any of the Etna's activity states, including during eruptive periods.

4.4. Tracking Volume Changes in the Magma Reservoir

The cumulative volumes of erupted (output) and degassed (input) magma during late-2015 to 2024 are respectively 124 ± 34 Mm^3 and 777 ± 256 Mm^3 (Figures 7b and 7c). These values imply that only ∼16% of the supplied magma is discharged during eruptions, providing a first-order estimate of eruption efficiency.

Models of the plumbing systems of persistently active open-vent volcanoes (Shinohara, 2008; Stevenson & Blake, 1998) suggest that, during background activity (the "equilibrium state" of Laiolo et al., 2022), magma input into the shallow plumbing system is compensated by magma recycled back into the deep plumbing system as dense degassed magma, so that no shallow accumulation of magma occurs. If we subtract a baseline (background activity) magma input/degassing rate of 1.18 m^3/s, corresponding to the quiescent phase of mid-2017–2018 (green shaded area in Figures 6 and 7, when both thermal and SO_2 fluxes were at their lowest levels), the magma input volume reduces to 437 ± 145 Mm^3 (black solid line in Figure 7c). This eruptible magma volume (see also Laiolo et al., 2022) corresponds to the volume of magma in excess to that sustaining background (baseline) activity (as exemplified by the quiescent phase of mid-2017–2018) that, accumulating in the shallow plumbing system, is ultimately available to sustain eruptive activity. With an erupted magma volume of 124 ± 34 Mm^3, we estimate that ∼28% of the eruptible input magma volume (437 ± 145 Mm^3) is ultimately erupted, whilst the remaining magma fraction (∼72%) remains stored/stalled within the plumbing system. For

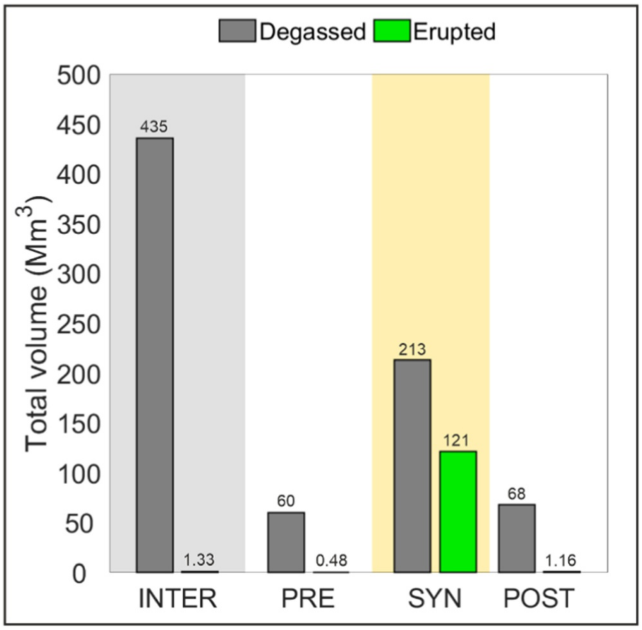

Figure 8. Total degassed and erupted magma volumes obtained by cumulating the daily input and output magma rates during the inter-event (gray area) and pre-, syn- (orange area) and post-eruptive periods.

comparison, Palano et al. (2024) inferred the magma eruption efficiency during 2001–2021 to be ∼29% based on ground deformation records. It is important to recall in this context that ground deformation records are sensitive to net volume changes within the shallow plumbing system, and hence miss the contribution of steady-state magma transfer, in which magma input is compensated by magma output (as dense recycled magma).

The difference between the eruptible magma volume (437 ± 145 Mm^3; calculated above) and the erupted magma volume (124 ± 34 Mm^3; from thermal records) corresponds to the "excess" magma volume, that is, the volume that would have accumulated within the Etna's magma plumbing system. This "excess" magma volume, shown in Figure 9a, reveals a steady increase, implying that magma accumulation prevails over magma withdrawal (e.g., that more magma enters the system than it is emitted during eruption). In particular, the "excess" magma volume reaches ∼120 Mm^3 at the onset of the 2020–2021 paroxysmal sequences, when the subsequent inversion of the trend implies eruption of more magma than being supplied to the plumbing system, causing a net mass deficit (Figure 9a).

To test whether the alternations between magma accumulation and withdrawal are capable of producing measurable surface deformations, we compare our results with continuous GNSS (Global Navigation Satellite System) observations from the continuous geodetic network operating on Etna (Palano et al., 2023, 2024). GNSS stations continuously record the three-

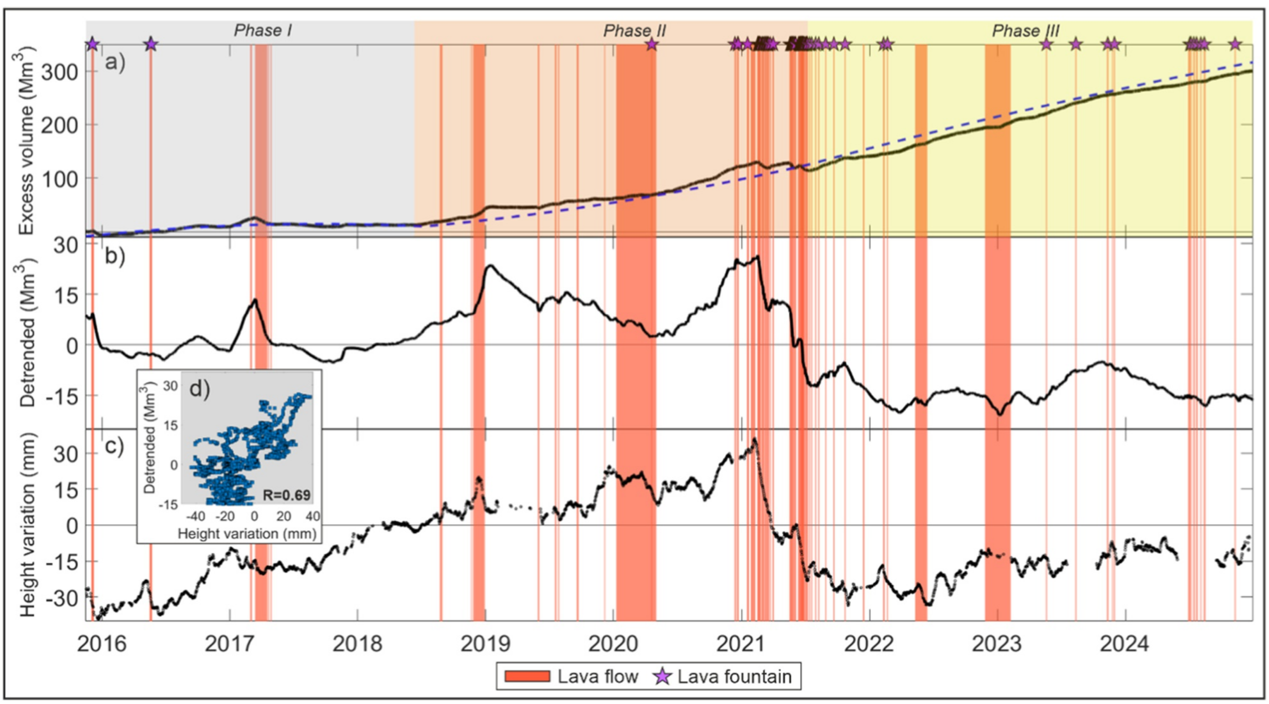

Figure 9. (a) Magma accumulation within Etna's shallow plumbing system during the observed period. This excess volume has been obtained by removing from the magma input rate the fixed recycling rate of 1.18 m^3/s and the magma output rate, and can be divided into three main periods: (i) a period dominated by passive degassing and low excess volumes (Phase I), (ii) a period of magma accumulation starting from late-2018 and culminating in the 2020–2021 lava fountain sequences (Phase II), and (iii) a period of less abundant eruptive events and restored magma accumulation (Phase III); (b) Polynomial detrending of the cumulative magma accumulation curve (panel "a"), performed removing distinct second-degree fits (blue dashed lines in panel "a"); (c) Height variations of the top of the volcanic edifice measured by the EPLU station (see also Palano et al., 2024); (d) Scatter-plot showing the positive correlation between the detrended excess volume curve and the volcano's height variations.

10.1029/2025GC012808

dimensional position of benchmarks installed on the volcano with millimetric precision, allowing subtle ground movements to be detected over time, such as outward and upward displacements during edifice inflation, and inward and downward motion during deflation, corresponding to magma accumulation and withdrawal, respectively. In particular, we use the time series of the vertical component of the EPLU station (Figure 9c), located close to the summit area (see Palano et al., 2024). Raw GNSS observations are processed by using the GAMIT/GLOBK software (http://geoweb.mit.edu/gg/) and framed within the local MERF23 reference system by adopting the same strategy described in Palano et al. (2023). Results (Figure 9c) indicate a general continuous inflation trend of the volcanic edifice from 2016 to early 2021, above which a sequence of shorter-scale inflation/deflation cycles are superimposed (e.g., in late 2016–early 2017; late 2018; early 2020; late 2020 to early 2021), corresponding to the main eruptive phase. This is followed by an abrupt deflation of the volcanic edifice during the 2021 eruptive sequence, and hence, a relative minor uplift from 2022 onward.

The deformation and magma supply/withdrawal patterns can be linked by comparing the GNSS-derived vertical displacements (Figure 9c) with the cumulative excess volume time series (Figure 9a). This latter shows distinct break-in-the-slopes that allow identifying three main Phases. Phase I, predominantly characterized by passive degassing and sporadic eruptive events, exhibits an excess volume curve with a relatively steady positive slope (gray interval, Figure 9a). This is followed by Phase II, in which a net increase in the slope of the excess volume curve marks a period of intensified eruptive activity that culminates in the 2020–2021 high-clustered lava fountain sequences (orange in Figure 9a). Notably, the large magma discharge at the end of Phase II produces a reversal in the excess volume trend (Figure 9a). Finally, the onset of Phase III (in yellow in Figure 9a) is identified as the time at which the excess volume curve restores a positive slope/trend.

To enable a quantitative comparison between the excess volume and the GNSS-derived deformation signal, we remove the long-term trend from the cumulative excess volume time series by fitting independent second-order polynomials to each of the three phases identified above. We caution that this detrending approach is not physically based (e.g., based on a specific process/phenomenon), but rather an attempt to resolve any short-term deviation from the long-term magma supply versus output balance. These independently inferred deviations can hence be compared with the GNSS-derived ground deformation trend that primarily reflects net volume changes within the shallow plumbing system. We caution that the strength of the correlation obtained is highly dependent on the selected detrending function. Use of alternative approaches, including linear and second-order polynomials applied over the entire (not divided into phases) time series, or a segmented linear detrending, is illustrated in Figure S12 in Supporting Information S1. These tests show that the correlation decreases when the time series is not segmented according to the main inflection points of the cumulative excess volume curve, and that it improves when non-linear detrending approaches are adopted, as these better capture the intrinsic variability of the cumulative signal. Part of the long-term trend may additionally reflect magma storage processes that are not fully captured by the vertical GNSS component alone, including possible lateral magma accumulation within the plumbing system (Palano et al., 2024). Non-linear detrending functions may therefore better approximate the intrinsic variability of the cumulative excess volume signal compared to simpler linear approaches.

With these limitations in mind, our results suggest that the detrended excess volume time series (Figure 9b) is positively correlated with the vertical displacement recorded at the EPLU station (Figures 9c and 9d), hence corroborating a link between input/output imbalance and summit deformation. We find that, between 2016 and the start of the 2020–2021 paroxysmal sequences, the edifice underwent a net uplift of ∼60 mm, in general agreement with the volumetric accumulation trend inferred from our SO_2-thermal budget (Figures 9a and 9b). The 2020–2021 lava fountain events (Aiuppa et al., 2023; Amadio et al., 2024; Carleo et al., 2023; Marchese et al., 2021) produced both a reversal in the elevation trend (∼60 mm of subsidence until the end of 2021) and in the magma budget curves (Figure 9). According to Palano et al. (2024), these deformation changes can be explained by a deflating source located at ∼6 km depth b.s.l. After this period, the occurrence of more sporadic lava fountains interspersed by sustained passive degassing, produced a less pronounced subsidence of the volcano, resuming a general slight volume accumulation. These correspondences underscore the value of the combined thermal-gas approach to trace endogenous accumulation processes of eruptible magma in volcanic systems, with clear implications for hazard assessment.

10.1029/2025GC012808

4.5. A Valuable Monitoring Tool—With Caveats and Limitations

We have provided evidence for the utility of a combined SO_2-thermal approach to understand Etna's behavior, and to track (and potentially anticipate) the quiescence-to-eruption transition. This combined approach is also relevant to understanding the volcano magma budget (cfr. 4.3 and 4.4). Our analysis, however, also demonstrates the caveats and limits of the UV Camera-derived SO_2 flux time-series as a volcano monitoring tool.

We have shown that the UV Camera-derived SO_2 flux records can resolve *some*, but not *all*, of Etna's eruptive phases (Figure 5) and that larger eruptions are more frequently associated with periods of above-background SO_2 degassing (Figure 5c). This means that while major swings in volcanic activity can be effectively tracked (and potentially anticipated; see also Figure 6 and related discussion on "orange" periods), our UV Camera network appears to be unsuitable for identifying *any* change in Etna's activity state, especially those associated with small (<1 Mm^3) erupted volumes (Figure 5c). This limit may not only apply to UV Camera records but also to SO_2 flux time series in general. Notably, at open-vent, persistently active volcanoes such as Etna, the large (in the order of a thousand tonnes/day) SO_2 emissions during background (quiescent) activity render small perturbation of the magma feeding system difficult, or even impossible, to detect. This likely applies to the majority of the large volcanic gas emitters on Earth (Aiuppa et al., 2019; Carn et al., 2017).

However, some caveats and limits are characteristic of the UV Camera technique. For example, our camera system is blind to any degassing/eruption process occurring in the central/northern portion of the crater terrace; hence, any eruption at NEC and (partially) at VOR would remain undetected. Given the preferential clustering of volcanic activity at SEC during late-2015 to 2024 (Figure 2a), this is unlikely to be a severe limit in our specific case. More difficult to evaluate is the impact of processes related to radiative transfer issues. SO_2 fluxes derived from UV Cameras are affected by multiple factors, including multiple scattering in the plume and in the background atmosphere, light dilution, in-plume condensation processes, and changes in atmospheric conditions and wind pattern, all of which introduce significant uncertainties and lead to potential underestimation of SO_2 (Delle Donne et al., 2022; Kern, 2025; Kern, Deutschmann, et al., 2010; Kern, Kick, et al., 2010; Kern et al., 2013; Lo Bue Trisciuzzi et al., 2024). These problems are exacerbated using a single high-elevation station, where plume geometry and atmospheric conditions can strongly influence the acquired signal, especially in a multi-vent and high-elevation volcano like Etna. In our specific case, the use of operator-reviewed images can mitigate against errors associated with multiple scattering, by selecting frames associated to the best viewing conditions, such as ash-poor plumes or favorable (cloud-free) meteorological settings. Nevertheless, this operation addresses only a limited fraction of the uncertainties, while additional processes, such as light dilution, still affect the measurements (cfr. 2.1).

Furthermore, several practical limitations arise when operating a single UV Camera station over long periods. These include instrumental malfunctions and the need for periodic maintenance, such as retrieving data from saturated hard disks and replacing them, as well as ensuring a continuous power supply. In addition, regular monitoring of both station components and acquired images is required to guarantee system reliability over long-term deployments. However, the fact that the station is installed within a protected INGV monitoring shelter provides a controlled environment, enabling sustained long-term operation and continuous data acquisition. Manual inspection and filtering of acquired images further represent an essential step, as several issues may arise at the summit site. These include snow or ice accumulation on the camera window, which can partially or completely obscure the field of view, as well as ash-rich plumes during lava fountain events.

A further limitation is related to plume geometry and viewing conditions. Under strong-wind conditions, the complex morphology of the SEC ridge can cause the UV Camera-imaged plume to represent only part of the degassing process rather than its full extent. For this reason, evaluating the SO_2 flux dynamics using a single UV Camera station is a complex task, particularly when comparing different eruptive phenomena in terms of source characteristics and duration.

With these limitations in mind, the ability of the UV Camera system to resolve the eruptive degassing escalation from the quiescent level (Figures 5 and 6) proves its utility as a volcanic gas monitoring tool.

5. Conclusions

This study has provided a nearly decade-long synthesis of the degassing and thermal dynamics across the main eruptive phases of Mt. Etna, obtained through the joint analysis of SO_2 fluxes from a permanent UV Camera system and satellite-derived thermal radiance data.

We have shown that the thermal and SO_2 fluxes vary coherently across the different volcanic activity states. By analyzing the SO_2 and thermal records in proximity of 18 major eruptive phases from November 2015 to 2024, accounting for >90% of the erupted lava volume during the decade, we have inferred a characteristic progression of increasing SO_2 fluxes, from 1,957 ± 1,470 t/d during the inter-eruptive periods, to 2,302 ± 1,481 t/d in the (15 days-long) pre-eruptive periods, and up to 3,828 ± 2,686 t/d during eruption. The SO_2 fluxes then decay to 2,595 ± 1,929 t/d in the post-eruptive period. Likewise, the transition from quiescence activity to more energetic behavior is associated with thermal fluxes >0.3 GW, with the most energetic eruptive episodes typically radiating more than 1 GW.

We tested the ability of the UV Camera-derived SO_2 fluxes to resolve the different Etna's activity states, finding above-background degassing conditions in the 61%, ~72%, and 72% of pre-, syn- and post-eruptive periods. These fractions scale with eruption magnitude, implying that larger eruptions are associated with major swings in activity that can be more effectively captured (and frequently anticipated by several days) in the SO_2 record, while less voluminous eruptive phases more frequently escape from detection. This analysis reveals the benefits and applicability limits of UV Cameras as monitoring tools.

We have also resolved the magma input (degassing) and output (eruption) volumetric fluxes associated with the inter-, pre-, syn- and post-eruptive periods. Results indicate that eruptive phases are initiated by magma input rates increasing well above the inter-eruptive average of 2.198 ± 0.726 m^3/s. Our volumetric analysis confirms that the significant imbalance between degassed and erupted magma extends across all activity phases, and is highest during inter-eruptive periods (~0.4% of degassing magma being erupted) and lowest during eruption (~60% of degassing magma being erupted). Over a nearly decade of activity, the erupted magma fraction is ~28%, with the residual fraction of unerupted magma (~120 Mm^3 from 2016 at the onset of the 2021 large lava fountain sequences) being stored in the plumbing system. However, these values should be considered as minimum estimates, as the UV Camera system may be affected by light dilution underestimations and may not always capture the entire gas plume due to field-of-view limitations under variable wind conditions. Furthermore, the estimated accumulated magma volume within the Etna's magma plumbing system shows coherent fluctuations with vertical ground displacement of the volcano edifice. This reveals the value of the combined thermal-gas approach to trace endogenous accumulation processes of eruptible magma in volcanic systems.

The in-tandem analysis of SO_2 and thermal flux data can contribute to a deeper understanding of gas and magma budgets at open-vent volcanoes globally. A further advance would also incorporate continuous GNSS data, which has provided robust constraints on magma budget estimates at several active volcanoes worldwide.

Acknowledgments

This study received funding from the European Union Next-Generation EU (National Recovery and Resilience Plan—NRRP, Mission 4, Component 2, Investment 1.3—D.D. 1243 2/8/2022, PE0000005) within the RETURN Extended Partnership. AA also received funding from the European Research Council under the European Union's Seventh Framework Program (FP7/2007/2013)/ERC grant agreement 305377 (BRIDGE Project). GG and GB thank the INGV project Pianeta Dinamico (CUP D53J19000170001) funded by MIUR ("Fondo finalizzato al rilancio degli investimenti delle amministrazioni centrali dello Stato e allo sviluppo del Paese," legge 145/2018), VT-SAFARI, Scientific Responsibility: G.G. Open access publishing facilitated by Universita degli Studi di Palermo, as part of the Wiley - CRUI-CARE agreement.

Conflict of Interest

The authors declare no conflicts of interest relevant to this study.

Availability Statement

All data sets used for the analyses presented in this study, including daily averaged SO_2 fluxes, GNSS measurements and thermal data, are publicly available in the Zenodo repository via Lo Bue Trisciuzzi (2025). Raw UV Camera imagery is not archived due to its large size, but is accessible through the respective data providers and institutional repositories.

References

Aiuppa, A., Agusto, M., Allard, P., Carn, S., De Moor, J. M., Inguaggiato, S., et al. (2025). Geochemical volcano monitoring. https://doi.org/10.31223/X5TT6D

Aiuppa, A., Caudron, C., Chiodini, G., Ingebritsen, S., & Viveiros, F. (2025). Geochemical monitoring of volcanic fluids in the twenty-first century. In Z. Spica & C. Caudron (A c. Di) (Eds.), *Modern volcano monitoring* (pp. 209–260). Springer Nature. https://doi.org/10.1007/978-3-031-86841-2_8

Aiuppa, A., De Moor, J. M., Arellano, S., Coppola, D., Francofonte, V., Galle, B., et al. (2018). Tracking formation of a lava lake from ground and space: Masaya Volcano (Nicaragua), 2014–2017. *Geochemistry, Geophysics, Geosystems*, *19*(2), 496–515. https://doi.org/10.1002/2017GC007227

Aiuppa, A., Fischer, T. P., Plank, T., & Bani, P. (2019). CO_2 flux emissions from the Earth's most actively degassing volcanoes, 2005–2015. *Scientific Reports*, *9*(1), 5442. https://doi.org/10.1038/s41598-019-41901-y

Aiuppa, A., Lo Bue Trisciuzzi, G., Alparone, S., Bitetto, M., Coltelli, M., Delle Donne, D., et al. (2023). A SO_2 flux study of the Etna volcano 2020–2021 paroxysmal sequences. *Frontiers in Earth Science*, *11*, 1115111. https://doi.org/10.3389/feart.2023.1115111

Allard, P. (1997). Endogenous magma degassing and storage at Mount Etna. *Geophysical Research Letters*, *24*(17), 2219–2222. https://doi.org/10.1029/97GL02101

Allard, P., Behncke, B., D'Amico, S., Neri, M., & Gambino, S. (2006). Mount Etna 1993–2005: Anatomy of an evolving eruptive cycle. *Earth-Science Reviews*, *78*(1–2), 85–114. https://doi.org/10.1016/j.earscirev.2006.04.002

Amadio, F., Pioli, L., & Scollo, S. (2024). Constraining proximal grainsize distribution of tephra from paroxysmal eruptions at Etna volcano. *Journal of Volcanology and Geothermal Research*, *454*, 108164. https://doi.org/10.1016/j.jvolgeores.2024.108164

Andronico, D., Behncke, B., De Beni, E., Cristaldi, A., Scollo, S., Lopez, M., & Lo Castro, M. D. (2018). Magma budget from lava and tephra volumes erupted during the 25-26 October 2013 lava fountain at Mt Etna. *Frontiers in Earth Science*, *6*, 116. https://doi.org/10.3389/feart.2018.00116

Andronico, D., Branca, S., Calvari, S., Burton, M., Caltabiano, T., Corsaro, R. A., et al. (2005). A multi-disciplinary study of the 2002-03 Etna eruption: Insights into a complex plumbing system. *Bulletin of Volcanology*, *67*(4), 314–330. https://doi.org/10.1007/s00445-004-0372-8

Andronico, D., Cannata, A., Di Grazia, G., & Ferrari, F. (2021). The 1986–2021 paroxysmal episodes at the summit craters of Mt. Etna: Insights into volcano dynamics and hazard. *Earth-Science Reviews*, *220*, 103686. https://doi.org/10.1016/j.earscirev.2021.103686

Arellano, S., Galle, B., Apaza, F., Avard, G., Barrington, C., Bobrowski, N., et al. (2021). Synoptic analysis of a decade of daily measurements of SO_2 emission in the troposphere from volcanoes of the global ground-based Network for Observation of Volcanic and Atmospheric Change. *Earth System Science Data*, *13*(3), 1167–1188. https://doi.org/10.5194/essd-13-1167-2021

Behncke, B., & Neri, M. (2003). Cycles and trends in the recent eruptive behaviour of Mount Etna (Italy). *Canadian Journal of Earth Sciences*, *40*(10), 1405–1411. https://doi.org/10.1139/e03-052

Bluth, G. J. S., Shannon, J. M., Watson, I. M., Prata, A. J., & Realmuto, V. J. (2007). Development of an ultra-violet digital camera for volcanic SO_2 imaging. *Journal of Volcanology and Geothermal Research*, *161*(1–2), 47–56. https://doi.org/10.1016/j.jvolgeores.2006.11.004

Boichu, M., Clarisse, L., Péré, J.-C., Herbin, H., Goloub, P., Thieuleux, F., et al. (2015). Temporal variations of flux and altitude of sulfur dioxide emissions during volcanic eruptions: Implications for long-range dispersal of volcanic clouds. *Atmospheric Chemistry and Physics*, *15*(14), 8381–8400. https://doi.org/10.5194/acp-15-8381-2015

Bonaccorso, A., Caltabiano, T., Currenti, G., Del Negro, C., Gambino, S., Ganci, G., et al. (2011). Dynamics of a lava fountain revealed by geophysical, geochemical and thermal satellite measurements: The case of the 10 April 2011 Mt Etna eruption: Lava fountain multidisciplinary approach. *Geophysical Research Letters*, *38*(24). https://doi.org/10.1029/2011GL049637

Bonaccorso, A., Carleo, L., Currenti, G., & Sicali, A. (2021). Magma migration at shallower levels and lava fountains sequence as revealed by borehole dilatometers on Etna Volcano. *Frontiers in Earth Science*, *9*, 740505. https://doi.org/10.3389/feart.2021.740505

Bonaccorso, A., Currenti, G., Linde, A., & Sacks, S. (2013). New data from borehole strainmeters to infer lava fountain sources (Etna 2011–2012). *Geophysical Research Letters*, *40*(14), 3579–3584. https://doi.org/10.1002/grl.50692

Branca, S., Coltelli, M., Groppelli, G., & Lentini, F. (2011). Geological map of Etna volcano, 1:50,000 scale. *Italian Journal of Geosciences*, *130*(3), 265–291. https://doi.org/10.3301/IJG.2011.15

Branca, S., & Del Carlo, P. (2004). Eruptions of Mt. Etna during the past 3,200 Years: A revised compilation integrating the historical and stratigraphic records. In A. Bonaccorso, S. Calvari, M. Coltelli, C. Del Negro, & S. Falsaperla (A. c. Di) (Eds.), *Geophysical monograph series* (Vol. 143, pp. 1–27). American Geophysical Union. https://doi.org/10.1029/143GM02

Branca, S., & Del Carlo, P. D. (2005). Types of eruptions of Etna volcano AD 1670–2003: Implications for short-term eruptive behaviour. *Bulletin of Volcanology*, *67*(8), 732–742. https://doi.org/10.1007/s00445-005-0412-z

Bruno, V., Aloisi, M., Gambino, S., Mattia, M., Ferlito, C., & Rossi, M. (2022). The most intense deflation of the last two decades at Mt. Etna: The 2019–2021 evolution of ground deformation and modeled pressure sources. *Geophysical Research Letters*, *49*(6), e2021GL095195. https://doi.org/10.1029/2021GL095195

Burton, M. R., Salerno, G. G., D'Auria, L., Caltabiano, T., Murè, F., & Maugeri, R. (2015). SO_2 flux monitoring at Stromboli with the new permanent INGV SO_2 camera system: A comparison with the FLAME network and seismological data. *Journal of Volcanology and Geothermal Research*, *300*, 95–102. https://doi.org/10.1016/j.jvolgeores.2015.02.006

Calvari, S., Biale, E., Bonaccorso, A., Cannata, A., Carleo, L., Currenti, G., et al. (2022). Explosive paroxysmal events at Etna volcano of different magnitude and intensity explored through a multidisciplinary monitoring system. *Remote Sensing*, *14*(16), 4006. https://doi.org/10.3390/rs14164006

Calvari, S., Bonaccorso, A., & Ganci, G. (2021). Anatomy of a paroxysmal lava fountain at Etna volcano: The case of the 12 March 2021, episode. *Remote Sensing*, *13*(15), 3052. https://doi.org/10.3390/rs13153052

Calvari, S., Ganci, G., Victória, S., Hernandez, P., Perez, N., Barrancos, J., et al. (2018). Satellite and ground remote sensing techniques to trace the hidden growth of a lava flow field: The 2014–2015 effusive eruption at Fogo Volcano (Cape Verde). *Remote Sensing*, *10*(7), 1115. https://doi.org/10.3390/rs10071115

Campion, R., Delgado-Granados, H., Legrand, D., Taquet, N., Boulesteix, T., Pedraza-Espitía, S., & Lecocq, T. (2018). Breathing and coughing: The extraordinarily high degassing of Popocatépetl Volcano investigated with an SO_2 camera. *Frontiers in Earth Science*, *6*, 163. https://doi.org/10.3389/feart.2018.00163

Campion, R., Delgado-Granados, H., & Mori, T. (2015). Image-based correction of the light dilution effect for SO_2 camera measurements. *Journal of Volcanology and Geothermal Research*, *300*, 48–57. https://doi.org/10.1016/j.jvolgeores.2015.01.004

Cannata, A., Di Grazia, G., Giuffrida, M., Gresta, S., Palano, M., Sciotto, M., et al. (2018). Space-time evolution of magma storage and transfer at Mt. Etna Volcano (Italy): The 2015–2016 reawakening of Voragine Crater. *Geochemistry, Geophysics, Geosystems*, *19*(2), 471–495. https://doi.org/10.1002/2017GC007296

Carleo, L., Currenti, G., & Bonaccorso, A. (2023). Clustering of eruptive events from high-precision strain signals recorded during the 2020–2022 lava fountains at the Etna volcano (Italy). *Natural Hazards and Earth System Sciences*, *23*(5), 1743–1754. https://doi.org/10.5194/nhess-23-1743-2023

Carn, S. A., Clarisse, L., & Prata, A. J. (2016). Multi-decadal satellite measurements of global volcanic degassing. *Journal of Volcanology and Geothermal Research*, *311*, 99–134. https://doi.org/10.1016/j.jvolgeores.2016.01.002

Carn, S. A., Fioletov, V. E., McLinden, C. A., Li, C., & Krotkov, N. A. (2017). A decade of global volcanic SO_2 emissions measured from space. *Scientific Reports*, *7*(1), 44095. https://doi.org/10.1038/srep44095

Coppola, D., Laiolo, M., Massimetti, F., & Cigolini, C. (2019). Monitoring endogenous growth of open-vent volcanoes by balancing thermal and SO_2 emissions data derived from space. *Scientific Reports*, *9*(1), 9394. https://doi.org/10.1038/s41598-019-45753-4

Corradini, S., Guerrieri, L., Stelitano, D., Salerno, G., Scollo, S., Merucci, L., et al. (2020). Near real-time monitoring of the Christmas 2018 Etna eruption using SEVIRI and products validation. *Remote Sensing*, *12*(8), 1336. https://doi.org/10.3390/rs12081336

Corsaro, R. A., Andronico, D., Behncke, B., Branca, S., Caltabiano, T., Ciancitto, F., et al. (2017). Monitoring the December 2015 summit eruptions of Mt. Etna (Italy): Implications on eruptive dynamics. *Journal of Volcanology and Geothermal Research*, *341*, 53–69. https://doi.org/10.1016/j.jvolgeores.2017.04.018

D'Aleo, R., Bitetto, M., Delle Donne, D., Coltelli, M., Coppola, D., McCormick Kilbride, B., et al. (2019). Understanding the SO_2 degassing budget of Mt Etna's paroxysms: First clues from the December 2015 sequence. *Frontiers in Earth Science*, *6*, 239. https://doi.org/10.3389/feart.2018.00239

D'Aleo, R., Bitetto, M., Delle Donne, D., Tamburello, G., Battaglia, A., Coltelli, M., et al. (2016). Spatially resolved SO_2 flux emissions from Mt Etna. *Geophysical Research Letters*, *43*(14), 7511–7519. https://doi.org/10.1002/2016GL069938

Delbrel, J., Burton, M., Esse, B., Hayer, C., & Varnam, M. (2024). TROPOMI/PlumeTraj SO_2 fluxes consistent with partially degassed magma supplying the 2018 Kīlauea eruption. *Journal of Volcanology and Geothermal Research*, *450*, 108066. https://doi.org/10.1016/j.jvolgeores.2024.108066

Delle Donne, D., Aiuppa, A., Bitetto, M., D'Aleo, R., Coltelli, M., Coppola, D., et al. (2019). Changes in SO_2 flux regime at Mt. Etna captured by automatically processed ultraviolet camera data. *Remote Sensing*, *11*(10), 1201. https://doi.org/10.3390/rs11101201

Delle Donne, D., Lo Coco, E., Bitetto, M., La Monica, F. P., Lacanna, G., Lages, J., et al. (2022). Spatio-temporal changes in degassing behavior at Stromboli volcano derived from two co-exposed SO_2 camera stations. *Frontiers in Earth Science*, *10*, 972071. https://doi.org/10.3389/feart.2022.972071

Delle Donne, D., Tamburello, G., Aiuppa, A., Bitetto, M., Lacanna, G., D'Aleo, R., & Ripepe, M. (2017). Exploring the explosive-effusive transition using permanent ultraviolet cameras. *Journal of Geophysical Research: Solid Earth*, *122*(6), 4377–4394. https://doi.org/10.1002/2017JB014027

Del Negro, C., Cappello, A., & Ganci, G. (2016). Quantifying lava flow hazards in response to effusive eruption. *Geological Society of America Bulletin*, *128*(5–6), 752–763. https://doi.org/10.1130/B31364.1

Del Negro, C., Currenti, G., Solaro, G., Greco, F., Pepe, A., Napoli, R., et al. (2013). Capturing the fingerprint of Etna volcano activity in gravity and satellite radar data. *Scientific Reports*, *3*(1), 3089. https://doi.org/10.1038/srep03089

Dragoni, M., & Tallarico, A. (2009). Assumptions in the evaluation of lava effusion rates from heat radiation. *Geophysical Research Letters*, *36*(8), 2009GL037411. https://doi.org/10.1029/2009GL037411

Edmonds, M. (2021). Geochemical monitoring of volcanoes and the mitigation of volcanic gas hazards. In *Forecasting and planning for volcanic hazards, risks, and disasters* (pp. 117–151). Elsevier. https://doi.org/10.1016/B978-0-12-818082-2.00004-4

Edmonds, M., Liu, E. J., & Cashman, K. V. (2022). Open-vent volcanoes fuelled by depth-integrated magma degassing. *Bulletin of Volcanology*, *84*(3), 28. https://doi.org/10.1007/s00445-021-01522-8

Edmonds, M., & Wallace, P. J. (2017). Volatiles and exsolved vapor in volcanic systems. *Elements*, *13*(1), 29–34. https://doi.org/10.2113/gselements.13.1.29

Fischer, T. P., Arellano, S., Carn, S., Aiuppa, A., Galle, B., Allard, P., et al. (2019). The emissions of CO_2 and other volatiles from the world's subaerial volcanoes. *Scientific Reports*, *9*(1), 18716. https://doi.org/10.1038/s41598-019-54682-1

Francis, P., Oppenheimer, C., & Stevenson, D. (1993). Endogenous growth of persistently active volcanoes. *Nature*, *366*(6455), 554–557. https://doi.org/10.1038/366554a0

Galle, B., Oppenheimer, C., Geyer, A., McGonigle, A. J. S., Edmonds, M., & Horrocks, L. (2003). A miniaturised ultraviolet spectrometer for remote sensing of SO_2 fluxes: A new tool for volcano surveillance. *Journal of Volcanology and Geothermal Research*, *119*(1–4), 241–254. https://doi.org/10.1016/S0377-0273(02)00356-6

Ganci, G., Bilotta, G., Cappello, A., Herault, A., & Del Negro, C. (2016). HOTSAT: A multiplatform system for the thermal monitoring of volcanic activity using satellite data. *Geological Society, London, Special Publications*, *426*(1), 207–221. https://doi.org/10.1144/SP426.21

Ganci, G., Bilotta, G., Zuccarello, F., Calvari, S., & Cappello, A. (2023). A multi-sensor satellite approach to characterize the volcanic deposits emitted during Etna's lava fountaining: The 2020–2022 study case. *Remote Sensing*, *15*(4), 916. https://doi.org/10.3390/rs15040916

Ganci, G., Cappello, A., Bilotta, G., & Del Negro, C. (2020). How the variety of satellite remote sensing data over volcanoes can assist hazard monitoring efforts: The 2011 eruption of Nabro volcano. *Remote Sensing of Environment*, *236*, 111426. https://doi.org/10.1016/j.rse.2019.111426

Ganci, G., Cappello, A., Bilotta, G., Herault, A., Zago, V., & Del Negro, C. (2018). Mapping volcanic deposits of the 2011–2015 Etna eruptive events using satellite remote sensing. *Frontiers in Earth Science*, *6*, 83. https://doi.org/10.3389/feart.2018.00083

Ganci, G., Cappello, A., Zago, V., Bilotta, G., Herault, A., & Del Negro, C. (2018). 3D Lava flow mapping of the 17–25 May 2016 Etna eruption using tri-stereo optical satellite data. *Annals of Geophysics*, *61*(2), 3. https://doi.org/10.4401/ag-7875

Ganci, G., Harris, A. J. L., Del Negro, C., Guehenneux, Y., Cappello, A., Labazuy, P., et al. (2012). A year of lava fountaining at Etna: Volumes from SEVIRI. *Geophysical Research Letters*, *39*(6), 2012GL051026. https://doi.org/10.1029/2012GL051026

Ganci, G., James, M. R., Calvari, S., & Negro, C. D. (2013). Separating the thermal fingerprints of lava flows and simultaneous lava fountaining using ground-based thermal camera and SEVIRI measurements. *Geophysical Research Letters*, *40*(19), 5058–5063. https://doi.org/10.1002/grl.50983

Ganci, G., Vicari, A., Fortuna, L., & Negro, D. (2011). The HOTSAT volcano monitoring system based on combined use of SEVIRI and MODIS multispectral data. *Annals of Geophysics*, *54*(5), 18. https://doi.org/10.4401/ag-5338

Garel, F., Kaminski, E., Tait, S., & Limare, A. (2012). An experimental study of the surface thermal signature of hot subaerial isoviscous gravity currents: Implications for thermal monitoring of lava flows and domes. *Journal of Geophysical Research*, *117*(B2), 2011JB008698. https://doi.org/10.1029/2011JB008698

Gennaro, E., Iacono-Marziano, G., Paonita, A., Rotolo, S. G., Martel, C., Rizzo, A. L., et al. (2019). Melt inclusions track melt evolution and degassing of Etnean magmas in the last 15 ka. *Lithos*, *324–325*, 716–732. https://doi.org/10.1016/j.lithos.2018.11.023

Giuffrida, M., & Viccaro, M. (2017). Three years (2011–2013) of eruptive activity at Mt. Etna: Working modes and timescales of the modern volcano plumbing system from micro-analytical studies of crystals. *Earth-Science Reviews*, *171*, 289–322. https://doi.org/10.1016/j.earscirev.2017.06.003

Grandin, R., Boichu, M., Mathurin, T., & Pascal, N. (2024). Automatic estimation of daily volcanic sulfur dioxide gas flux from TROPOMI satellite observations: Application to Etna and Piton de la Fournaise. *Journal of Geophysical Research: Solid Earth*, *129*(6), e2024JB029309. https://doi.org/10.1029/2024JB029309

Greco, F., Bonforte, A., & Carbone, D. (2022). A long-term charge/discharge cycle at Mt. Etna volcano revealed through absolute gravity and GPS measurements. *Journal of Geodesy*, *96*(12), 101. https://doi.org/10.1007/s00190-022-01692-z

Harris, A., Favalli, M., Steffke, A., Fornaciai, A., & Boschi, E. (2010). A relation between lava discharge rate, thermal insulation, and flow area set using LiDAR data. *Geophysical Research Letters*, *37*(20), 2010GL044683. https://doi.org/10.1029/2010GL044683

Harris, A., Steffke, A., Calvari, S., & Spampinato, L. (2011). Thirty years of satellite-derived lava discharge rates at Etna: Implications for steady volumetric output. *Journal of Geophysical Research*, *116*(B8), B08204. https://doi.org/10.1029/2011JB008237

Harris, A. J. L., & Baloga, S. M. (2009). Lava discharge rates from satellite-measured heat flux. *Geophysical Research Letters*, *36*(19), 2009GL039717. https://doi.org/10.1029/2009GL039717

Harris, A. J. L., Blake, S., Rothery, D. A., & Stevens, N. F. (1997). A chronology of the 1991 to 1993 Mount Etna eruption using advanced very high resolution radiometer data: Implications for real-time thermal volcano monitoring. *Journal of Geophysical Research*, *102*(B4), 7985–8003. https://doi.org/10.1029/96JB03388

Harris, A. J. L., Dehn, J., & Calvari, S. (2007). Lava effusion rate definition and measurement: A review. *Bulletin of Volcanology*, *70*(1), 1–22. https://doi.org/10.1007/s00445-007-0120-y

Harris, A. J. L., Murray, J. B., Aries, S. E., Davies, M. A., Flynn, L. P., Wooster, M. J., et al. (2000). Effusion rate trends at Etna and Krafla and their implications for eruptive mechanisms. *Journal of Volcanology and Geothermal Research*, *102*(3–4), 237–269. https://doi.org/10.1016/S0377-0273(00)00190-6

Hirn, B. R., Di Bartola, C., Laneve, G., Cadau, E., & Ferrucci, F. (2008). SEVIRI onboard meteosat second generation, and the quantitative monitoring of effusive volcanoes in Europe and Africa. In *IGARSS 2008—2008 IEEE International Geoscience and Remote Sensing Symposium* (pp. III-374–III-377). https://doi.org/10.1109/IGARSS.2008.4779361

Ilanko, T., Pering, T. D., Wilkes, T. C., Woitischek, J., D'Aleo, R., Aiuppa, A., et al. (2020). Ultraviolet camera measurements of passive and explosive (Strombolian) sulphur dioxide emissions at Yasur Volcano, Vanuatu. *Remote Sensing*, *12*(17), 2703. https://doi.org/10.3390/rs12172703

Kahl, M., Chakraborty, S., Pompilio, M., & Costa, F. (2015). Constraints on the nature and evolution of the magma plumbing system of Mt. Etna Volcano (1991–2008) from a combined thermodynamic and kinetic modelling of the compositional record of minerals. *Journal of Petrology*, *56*(10), 2025–2068. https://doi.org/10.1093/petrology/egv063

Kantzas, E., & McGonigle, A. (2008). Ground based ultraviolet remote sensing of volcanic gas plumes. *Sensors*, *8*(3), 1559–1574. https://doi.org/10.3390/s8031559

Kazahaya, K., Shinohara, H., & Saito, G. (1994). Excessive degassing of Izu-Oshima volcano: Magma convection in a conduit. *Bulletin of Volcanology*, *56*(3), 207–216. https://doi.org/10.1007/BF00279605

Kazahaya, K., Shinohara, H., Uto, K., Odai, M., Nakahori, Y., Mori, H., et al. (2004). Gigantic SO_2 emission from Miyakejima volcano, Japan, caused by caldera collapse. *Geology*, *32*(5), 425. https://doi.org/10.1130/G20399.1

Kazahaya, R., Shinohara, H., Mori, T., Iguchi, M., & Yokoo, A. (2016). Pre-eruptive inflation caused by gas accumulation: Insight from detailed gas flux variation at Sakurajima volcano, Japan. *Geophysical Research Letters*, *43*(21). https://doi.org/10.1002/2016GL070727

Kern, C. (2025). Ultraviolet and visible remote sensing of volcanic gas emissions. *Journal of Volcanology and Geothermal Research*, *468*, 108423. https://doi.org/10.1016/j.jvolgeores.2025.108423

Kern, C., Aiuppa, A., & De Moor, J. M. (2022). A golden era for volcanic gas geochemistry? *Bulletin of Volcanology*, *84*(5), 43. https://doi.org/10.1007/s00445-022-01556-6

Kern, C., Deutschmann, T., Vogel, L., Wöhrbach, M., Wagner, T., & Platt, U. (2010). Radiative transfer corrections for accurate spectroscopic measurements of volcanic gas emissions. *Bulletin of Volcanology*, *72*(2), 233–247. https://doi.org/10.1007/s00445-009-0313-7

Kern, C., Deutschmann, T., Werner, C., Sutton, A. J., Elias, T., & Kelly, P. J. (2012). Improving the accuracy of SO_2 column densities and emission rates obtained from upward-looking UV-spectroscopic measurements of volcanic plumes by taking realistic radiative transfer into account. *Journal of Geophysical Research*, *117*(D20), 2012JD017936. https://doi.org/10.1029/2012JD017936

Kern, C., Kick, F., Lübcke, P., Vogel, L., Wöhrbach, M., & Platt, U. (2010). Theoretical description of functionality, applications, and limitations of SO_2 cameras for the remote sensing of volcanic plumes. *Atmospheric Measurement Techniques*, *3*(3), 733–749. https://doi.org/10.5194/amt-3-733-2010

Kern, C., Sutton, J., Elias, T., Lee, L., Kamibayashi, K., Antolik, L., & Werner, C. (2015). An automated SO_2 camera system for continuous, real-time monitoring of gas emissions from Kīlauea Volcano's summit Overlook Crater. *Journal of Volcanology and Geothermal Research*, *300*, 81–94. https://doi.org/10.1016/j.jvolgeores.2014.12.004

Kern, C., Werner, C., Elias, T., Sutton, A. J., & Lübcke, P. (2013). Applying UV cameras for SO_2 detection to distant or optically thick volcanic plumes. *Journal of Volcanology and Geothermal Research*, *262*, 80–89. https://doi.org/10.1016/j.jvolgeores.2013.06.009

Kunrat, S., Kern, C., Alfianti, H., & Lerner, A. H. (2022). Forecasting explosions at Sinabung Volcano, Indonesia, based on SO_2 emission rates. *Frontiers in Earth Science*, *10*, 976928. https://doi.org/10.3389/feart.2022.976928

Laiolo, M., Delle Donne, D., Coppola, D., Bitetto, M., Cigolini, C., Della Schiava, M., et al. (2022). Shallow magma dynamics at open-vent volcanoes tracked by coupled thermal and SO_2 observations. *Earth and Planetary Science Letters*, *594*, 117726. https://doi.org/10.1016/j.epsl.2022.117726

Lo Bue Trisciuzzi, G. (2025). Coupling UV camera-derived SO_2 fluxes and thermal output at Mount Etna: A decadal analysis across eruptive phases [Dataset]. *Zenodo*. https://doi.org/10.5281/zenodo.17599278

Lo Bue Trisciuzzi, G., Aiuppa, A., Salerno, G., Bitetto, M., Curcio, L., Innocenti, L., et al. (2024). Improved volcanic SO_2 flux records from integrated scanning-DOAS and UV Camera observations. *Journal of Volcanology and Geothermal Research*, *455*, 108207. https://doi.org/10.1016/j.jvolgeores.2024.108207

Lübcke, P., Bobrowski, N., Illing, S., Kern, C., Alvarez Nieves, J. M., Vogel, L., et al. (2013). On the absolute calibration of SO_2 cameras. *Atmospheric Measurement Techniques*, *6*(3), 677–696. https://doi.org/10.5194/amt-6-677-2013

Lucas, B. D., & Kanade, T. (1981). An iterative image registration technique with an application to stereo vision (Vol. *2*, pp. 674–679).

Marchese, F., Filizzola, C., Lacava, T., Falconieri, A., Faruolo, M., Genzano, N., et al. (2021). Mt. Etna paroxysms of February–April 2021 monitored and quantified through a multi-platform satellite observing system. *Remote Sensing*, *13*(16), 3074. https://doi.org/10.3390/rs13163074

McGonigle, A. J. S. (2007). Measurement of volcanic SO_2 fluxes with differential optical absorption spectroscopy. *Journal of Volcanology and Geothermal Research*, *162*(3–4), 111–122. https://doi.org/10.1016/j.jvolgeores.2007.02.001

Métrich, N., Allard, P., Spilliaert, N., Andronico, D., & Burton, M. (2004). 2001 flank eruption of the alkali- and volatile-rich primitive basalt responsible for Mount Etna's evolution in the last three decades. *Earth and Planetary Science Letters*, *228*(1–2), 1–17. https://doi.org/10.1016/j.epsl.2004.09.036

Métrich, N., Bertagnini, A., & Di Muro, A. (2010). Conditions of magma storage, degassing and ascent at Stromboli: New insights into the volcano plumbing system with inferences on the eruptive dynamics. *Journal of Petrology*, *51*(3), 603–626. https://doi.org/10.1093/petrology/egp083

Moretti, R., & Papale, P. (2004). On the oxidation state and volatile behavior in multicomponent gas–melt equilibria. *Chemical Geology*, *213*(1–3), 265–280. https://doi.org/10.1016/j.chemgeo.2004.08.048

Mori, T., & Burton, M. (2006). The SO_2 camera: A simple, fast and cheap method for ground-based imaging of SO_2 in volcanic plumes. *Geophysical Research Letters*, *33*(24), 2006GL027916. https://doi.org/10.1029/2006GL027916

Mori, T., & Burton, M. (2009). Quantification of the gas mass emitted during single explosions on Stromboli with the SO_2 imaging camera. *Journal of Volcanology and Geothermal Research*, *188*(4), 395–400. https://doi.org/10.1016/j.jvolgeores.2009.10.005

Mori, T., Shinohara, H., Kazahaya, K., Hirabayashi, J., Matsushima, T., Mori, T., et al. (2013). Time-averaged SO_2 fluxes of subduction-zone volcanoes: Example of a 32-year exhaustive survey for Japanese volcanoes. *Journal of Geophysical Research: Atmospheres*, *118*(15), 8662–8674. https://doi.org/10.1002/jgrd.50591

Nadeau, P. A., Palma, J. L., & Waite, G. P. (2011). Linking volcanic tremor, degassing, and eruption dynamics via SO_2 imaging. *Geophysical Research Letters*, *38*(1). https://doi.org/10.1029/2010GL045820

Oppenheimer, C., Fischer, T. P., & Scaillet, B. (2014). Volcanic degassing: Process and impact. In *Treatise on geochemistry* (pp. 111–179). Elsevier. https://doi.org/10.1016/B978-0-08-095975-7.00304-1

Oppenheimer, C., Scaillet, B., & Martin, R. S. (2011). Sulfur degassing from volcanoes: Source conditions, surveillance, plume chemistry and Earth system impacts. *Reviews in Mineralogy and Geochemistry*, *73*(1), 363–421. https://doi.org/10.2138/rmg.2011.73.13

Palano, M., Calcaterra, S., Gambino, P., Porfidia, B., & Sparacino, F. (2023). GNSS-based long-term deformation at Mount Etna volcano (Italy). *Results in Geophysical Sciences*, *14*, 100056. https://doi.org/10.1016/j.ringps.2023.100056

Palano, M., Pezzo, G., & Chiarabba, C. (2024). Magma budget, plutonic growth and lateral spreading at Mt. Etna. *Communications Earth & Environment*, *5*(1), 95. https://doi.org/10.1038/s43247-024-01267-0

Paonita, A., Liuzzo, M., Salerno, G., Federico, C., Bonfanti, P., Caracausi, A., et al. (2021). Intense overpressurization at basaltic open-conduit volcanoes as inferred by geochemical signals: The case of the Mt. Etna December 2018 eruption. *Science Advances*, *7*(36), eabg6297. https://doi.org/10.1126/sciadv.abg6297

Patanè, D., Aiuppa, A., Aloisi, M., Behncke, B., Cannata, A., Coltelli, M., et al. (2013). Insights into magma and fluid transfer at Mount Etna by a multiparametric approach: A model of the events leading to the 2011 eruptive cycle. *Journal of Geophysical Research: Solid Earth*, *118*(7), 3519–3539. https://doi.org/10.1002/jgrb.50248

Penndorf. (1957). Tables of the refractive index for standard air and the Rayleigh scattering coefficient for the spectral region between 02 and 200 μ and their application to atmospheric optics. *Journal of the Optical Society of America. A*, *47*, 176–182. https://doi.org/10.1364/josa.47.000176

Pering, T. D., Liu, E. J., Wood, K., Wilkes, T. C., Aiuppa, A., Tamburello, G., et al. (2020). Combined ground and aerial measurements resolve vent-specific gas fluxes from a multi-vent volcano. *Nature Communications*, *11*(1), 3039. https://doi.org/10.1038/s41467-020-16862-w

Pieri, D. C., & Baloga, S. M. (1986). Eruption rate, area, and length relationships for some Hawaiian lava flows. *Journal of Volcanology and Geothermal Research*, *30*(1–2), 29–45. https://doi.org/10.1016/0377-0273(86)90066-1

Queißer, M., Burton, M., Theys, N., Pardini, F., Salerno, G., Caltabiano, T., et al. (2019). TROPOMI enables high resolution SO_2 flux observations from Mt. Etna, Italy, and beyond. *Scientific Reports*, *9*(1), 957. https://doi.org/10.1038/s41598-018-37807-w

Reath, K., Pritchard, M., Poland, M., Delgado, F., Carn, S., Coppola, D., et al. (2019). Thermal, deformation, and degassing remote sensing time series (CE 2000–2017) at the 47 most active volcanoes in Latin America: Implications for volcanic systems. *Journal of Geophysical Research: Solid Earth*, *124*(1), 195–218. https://doi.org/10.1029/2018JB016199

Salerno, G., La Spina, A., Allard, P., Guerrieri, L., Corradini, S., Di Grazia, G., et al. (2025). The February–April 2021 sequence of lava fountain paroxysms on Mt Etna: Source mechanism deciphered from ground-based and satellite survey of volcanic gas emissions. *Bulletin of Volcanology*, *87*(11), 95. https://doi.org/10.1007/s00445-025-01877-2

Salerno, G. G., Burton, M. R., Oppenheimer, C., Caltabiano, T., Randazzo, D., Bruno, N., & Longo, V. (2009). Three-years of SO_2 flux measurements of Mt. Etna using an automated UV scanner array: Comparison with conventional traverses and uncertainties in flux retrieval. *Journal of Volcanology and Geothermal Research*, *183*(1–2), 76–83. https://doi.org/10.1016/j.jvolgeores.2009.02.013

Scaillet, B., Clemente, B., Evans, B. W., & Pichavant, M. (1998). Redox control of sulfur degassing in silicic magmas. *Journal of Geophysical Research*, *103*(B10), 23937–23949. https://doi.org/10.1029/98JB02301

Shinohara, H. (2008). Excess degassing from volcanoes and its role on eruptive and intrusive activity. *Reviews of Geophysics*, *46*(4), 2007RG000244. https://doi.org/10.1029/2007RG000244

Shinohara, H. (2013). Volatile flux from subduction zone volcanoes: Insights from a detailed evaluation of the fluxes from volcanoes in Japan. *Journal of Volcanology and Geothermal Research*, *268*, 46–63. https://doi.org/10.1016/j.jvolgeores.2013.10.007

Spilliaert, N., Allard, P., Métrich, N., & Sobolev, A. V. (2006). Melt inclusion record of the conditions of ascent, degassing, and extrusion of volatile-rich alkali basalt during the powerful 2002 flank eruption of Mount Etna (Italy). *Journal of Geophysical Research*, *111*(B4), 2005JB003934. https://doi.org/10.1029/2005JB003934

Spina, F., Bilotta, G., Cappello, A., Spina, M., Zuccarello, F., & Ganci, G. (2025). Volcanic activity classification through semi-supervised learning applied to satellite radiance time series. *Remote Sensing*, *17*(10), 1679. https://doi.org/10.3390/rs17101679

Steffke, A. M., Harris, A. J. L., Burton, M., Caltabiano, T., & Salerno, G. G. (2011). Coupled use of COSPEC and satellite measurements to define the volumetric balance during effusive eruptions at Mt. Etna, Italy. *Journal of Volcanology and Geothermal Research*, *205*(1–2), 47–53. https://doi.org/10.1016/j.jvolgeores.2010.06.004

Stevenson, D. S., & Blake, S. (1998). Modelling the dynamics and thermodynamics of volcanic degassing. *Bulletin of Volcanology*, *60*(4), 307–317. https://doi.org/10.1007/s004450050234

Tamburello, G., Aiuppa, A., Kantzas, E. P., McGonigle, A. J. S., & Ripepe, M. (2012). Passive vs. Active degassing modes at an open-vent volcano (Stromboli, Italy). *Earth and Planetary Science Letters*, *359–360*, 106–116. https://doi.org/10.1016/j.epsl.2012.09.050

Tamburello, G., Hansteen, T. H., Bredemeyer, S., Aiuppa, A., & Tassi, F. (2014). Gas emissions from five volcanoes in northern Chile and implications for the volatiles budget of the Central Volcanic Zone. *Geophysical Research Letters*, *41*(14), 4961–4969. https://doi.org/10.1002/2014GL060653

Tamburello, G., Kantzas, E. P., McGonigle, A. J. S., Aiuppa, A., & Giudice, G. (2011). UV camera measurements of fumarole field degassing (La Fossa crater, Vulcano Island). *Journal of Volcanology and Geothermal Research*, *199*(1–2), 47–52. https://doi.org/10.1016/j.jvolgeores.2010.10.004

Theys, N., Hedelt, P., De Smedt, I., Lerot, C., Yu, H., Vlietinck, J., et al. (2019). Global monitoring of volcanic SO_2 degassing with unprecedented resolution from TROPOMI onboard Sentinel-5 Precursor. *Scientific Reports*, *9*(1), 2643. https://doi.org/10.1038/s41598-019-39279-y

Vandaele, A. C., Simon, P. C., Guilmot, J. M., Carleer, M., & Colin, R. (1994). SO_2 absorption cross section measurement in the UV using a Fourier transform spectrometer. *Journal of Geophysical Research*, *99*(D12), 25599–25605. https://doi.org/10.1029/94JD02187

Viccaro, M., Garozzo, I., Cannata, A., Di Grazia, G., & Gresta, S. (2014). Gas burst vs. gas-rich magma recharge: A multidisciplinary study to reveal factors controlling triggering of the recent paroxysmal eruptions at Mt. Etna. *Journal of Volcanology and Geothermal Research*, *278–279*, 1–13. https://doi.org/10.1016/j.jvolgeores.2014.04.001

Wadge, G., & Guest, J. E. (1981). Steady-state magma discharge at Etna 1971–81. *Nature*, *294*(5841), 548–550. https://doi.org/10.1038/294548a0

Wadge, G., Walker, G. P. L., & Guest, J. E. (1975). The output of the Etna volcano. *Nature*, *255*(5507), 385–387. https://doi.org/10.1038/255385a0

Wallace, P. J., & Edmonds, M. (2011). The sulfur budget in magmas: Evidence from melt inclusions, submarine glasses, and volcanic gas emissions. *Reviews in Mineralogy and Geochemistry*, *73*(1), 215–246. https://doi.org/10.2138/rmg.2011.73.8

Werner, C., Kern, C., Coppola, D., Lyons, J. J., Kelly, P. J., Wallace, K. L., et al. (2017). Magmatic degassing, lava dome extrusion, and explosions from Mount Cleveland volcano, Alaska, 2011–2015: Insight into the continuous nature of volcanic activity over multi-year timescales. *Journal of Volcanology and Geothermal Research*, *337*, 98–110. https://doi.org/10.1016/j.jvolgeores.2017.03.001

Werner, C. A., Fischer, T., Aiuppa, A., Edmonds, M., Cardellini, C., Carn, S., et al. (2019). Carbon dioxide emissions from subaerial volcanic regions: Two decades in review. In B. Orcutt, D. Alvarez, & R. Dasgupta (A c. Di) (Eds.), *Deep carbon: Past to present* (pp. 188–236). Cambridge University Press; USGS Publications Warehouse. Retrieved from https://pubs.usgs.gov/publication/70261970

Wilkes, T. C., Pering, T. D., Aguilera, F., Layana, S., Nadeau, P., Kern, C., et al. (2023). A new permanent, low-cost, low-power SO_2 camera for continuous measurement of volcanic emissions. *Frontiers in Earth Science*, *11*, 1088992. https://doi.org/10.3389/feart.2023.1088992

Wright, R., Blake, S., Harris, A. J. L., & Rothery, D. A. (2001). A simple explanation for the space-based calculation of lava eruption rates. *Earth and Planetary Science Letters*, *192*(2), 223–233. https://doi.org/10.1016/S0012-821X(01)00443-5